# Laser-induced Periodic Surface Structures (LIPSS) on heavily boron-doped diamond for electrode applications

Frota Sartori, Andre; Orlando, Stefano; Bellucci, Alessandro; Trucchi, Daniele M.; Abrahami, Shoshan; Boehme, Thijs; Hantschel, Thomas; Vandervorst, Wilfried; Buijnsters, Josephus G.

**DOI**
10.1021/acsami.8b15951

**Publication date**
2018

**Document Version**
Final published version

**Published in**
ACS Applied Materials and Interfaces

ACS APPLIED MATERIALS & INTERFACES

Research Article

Cite This: ACS Appl. Mater. Interfaces 2018, 10, 43236−43251

www.acsami.org

# Laser-Induced Periodic Surface Structures (LIPSS) on Heavily Boron-Doped Diamond for Electrode Applications

André F. Sartori,*[,†] Stefano Orlando,[‡] Alessandro Bellucci,[‡] Daniele M. Trucchi,[‡] Shoshan Abrahami,[§] Thijs Boehme,[⊥,∥] Thomas Hantschel,[∥] Wilfried Vandervorst,[∥,⊥] and Josephus G. Buijnsters*[,†]

[†]Department of Precision and Microsystems Engineering, Research Group of Micro and Nano Engineering, Delft University of Technology, Mekelweg 2, 2628 CD Delft, The Netherlands

[‡]Istituto di Struttura della Materia (ISM), Unit of Montelibretti, Consiglio Nazionale delle Ricerche (CNR), Research Area of Rome 1, Via Salaria km 29.300, 00015 Monterotondo Scalo, Roma, Italy

[§]Department of Materials and Chemistry, Research Group Electrochemical and Surface Engineering (SURF), Vrije Universiteit Brussel, Pleinlaan 2, 1050 Brussels, Belgium

[∥]Imec, Kapeldreef 75, B-3001 Leuven, Belgium

[⊥]IKS-Department of Physics, KU Leuven, Celestijnenlaan 200D, B-3001 Leuven, Belgium

Supporting Information

**ABSTRACT:** Diamond is known as a promising electrode material in the fields of cell stimulation, energy storage (e.g., supercapacitors), (bio)sensing, catalysis, etc. However, engineering its surface and electrochemical properties often requires costly and complex procedures with addition of foreign material (e.g., carbon nanotube or polymer) scaffolds or cleanroom processing. In this work, we demonstrate a novel approach using laser-induced periodic surface structuring (LIPSS) as a scalable, versatile, and cost-effective technique to nanostructure the surface and tune the electrochemical properties of boron-doped diamond (BDD). We study the effect of LIPSS on heavily doped BDD and investigate its application as electrodes for cell stimulation and energy storage. We show that quasi-periodic ripple structures formed on diamond electrodes laser-textured with a laser accumulated fluence of 0.325 kJ/cm$^2$ (800 nm wavelength) displayed a much higher double-layer capacitance of 660 $\mu$F/cm$^2$ than the as-grown BDD (20 $\mu$F/cm$^2$) and that an increased charge-storage capacity of 1.6 mC/cm$^2$ (>6-fold increase after laser texturing) and a low impedance of 2.74 Ω cm$^2$ turn out to be appreciable properties for cell stimulation. Additional morphological and structural characterization revealed that ripple formation on heavily boron-doped diamond (2.8 atom % [B]) occurs at much lower accumulated fluences than the 2 kJ/cm$^2$ typically reported for lower doping levels and that the process involves stronger graphitization of the BDD surface. Finally, we show that the exposed interface between sp$^2$ and sp$^3$ carbon layers (i.e. the laser-ablated diamond surface) revealed faster kinetics than the untreated BDD in both ferrocyanide and RuHex mediators, which can be used for electrochemical (bio)sensing. Overall, our work demonstrates that LIPSS is a powerful single-step tool for the fabrication of surface-engineered diamond electrodes with tunable material, electrochemical, and charge-storage properties.

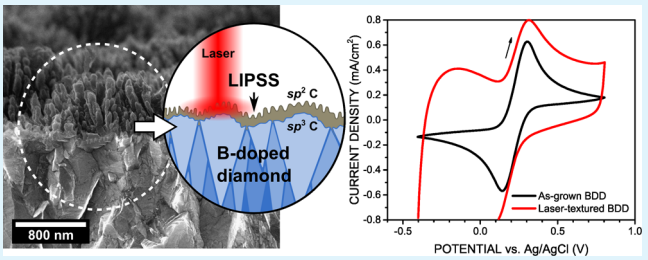


**KEYWORDS:** *boron-doped diamond, laser texturing, ripples, LIPSS, cyclic voltammetry, impedance spectroscopy, charge-storage capacity, supercapacitor*

## 1. INTRODUCTION

Interest in diamond has grown remarkably over the last years due to its superlative properties,[1−3] particularly in applications such as photonics and quantum information processing,[4,5] high-power high-frequency switching in electronics,[6] microelectromechanical systems (MEMS),[7,8] as hydrophobic coatings for microfluidic devices, as biocompatible substrates for cell proliferation in bioimplants,[9] in (bio)electrochemical sensors,[3,10] neural probes,[11] and supercapacitors,[12,13] to name a few. The use of nanostructured boron-doped diamond (BDD) for (bio)electrochemical sensing, cell stimulation, and energy storage in particular has been increasingly investigated,[13−15] thanks to diamond's chemically resilient, functionalizable, and biocompatible surface and also to the development of methods capable of enhancing the electrode's sensitivity, selectivity, and charge-storage/injection properties, through the modification of the BDD morphology, structure, and composition by top-down or bottom-up fabrication. Most of those strategies, however, either make use of complex and costly cleanroom processing (i.e., lithography and dry etching)

Received: September 13, 2018
Accepted: November 15, 2018
Published: November 15, 2018

or involve the addition of foreign materials, such as masks/templates, carbon nanotube or polymeric scaffolds, metal particles, etc.,[11,13,15−17] which are often unstable in the harsh growth environment during chemical vapor deposition (CVD) of diamond.[18] Another disadvantage of most methods is poor scalability for mass production. To overcome such limitations, we introduce the use of laser-induced periodic surface structuring (LIPSS)[19] as a promising single-step technique for the controlled surface engineering of diamond electrodes, down to the nanoscale, without the need for costly cleanroom processing or addition of foreign materials.[20]

Laser-induced periodic surface structures/structuring (LIPSS), laser texturing, or simply "ripples" consists of (quasi)periodic nanostructures formed on the surface of metals, semiconductors, or dielectric materials when irradiated by a polarized laser beam with high enough energy. This process typically gives rise to parallel lines with shape and periodicity that are strongly correlated with the laser wavelength, polarization, as well as laser fluence and the number of pulses.[19] With this technique, the formed nanostructures can be generated in a single-step process and allow the modification of the optical, mechanical, and chemical surface properties of the material. Additionally, LIPSS has the advantage that it can be performed in open environment and be easily incorporated into manufacture process flows, thus being an attractive alternative to costly vacuum- and cleanroom-based processing (e.g., lithography, dry etching, etc.) for the micro/nanostructuring of materials. Major fields of application are in the treatment of mostly metallic surfaces toward the control of color (due to diffraction), antireflective properties,[21] wettability (i.e., hydrophobicity/hydrophilicity),[22] antibacterial properties, as well as tribological properties (i.e., reduction of friction and wear). Thorough reviews on the mechanisms of LIPSS formation and its applications can be found here.[19,23]

The study and application of laser-textured diamond are still limited, with most of the reported works dating from 2014 onwards. LIPSS formation on diamond with ultrashort laser pulses was first demonstrated in 1999 by Ozkan et al.,[24] and later, Calvani et al. reported the modification of the optical properties of diamond films by femtosecond laser texturing[25] for the fabrication of photon-enhanced thermionic emission (PETE)-based devices.[26,27] More recent work has been done on the structural properties,[28] wettability,[29] conductivity,[30] and antireflective properties[31] of laser-textured diamond surfaces. LIPSS thus has the potential to enable a high degree of control over the performance and application of diamond-based (bio)electrochemical sensors and diamond electrodes in general, with the advantage of being a scalable and low-cost fabrication method.

In this paper, we present a thorough electrochemical characterization of BDD electrodes laser-textured by the LIPSS process under different conditions. We employed standard redox couples, ferrocyanide ($Fe(CN)_6^{3-/4-}$) and ruthenium hexamine ($Ru(NH_3)_6^{3+/2+}$), in aqueous solution and performed standard cyclic voltammetry (CV) and electrochemical impedance spectroscopy (EIS) measurements, to derive essential electrode parameters and quantitative figures for the electron-transfer kinetics for both mediators. The electrochemical investigation is complemented by morphological, structural, and surface characterization of the laser-textured BDD, performed by high-resolution field emission scanning electron microscopy (FE-SEM), Raman spectroscopy, contact angle measurement, and X-ray photoelectron spectroscopy (XPS). After the results are described, we analyze the effect of LIPSS on the electrochemical performance of the BDD electrodes in detail and discuss the potential use of laser-textured BDD for cell stimulation and recording applications, as well as for energy storage as supercapacitors, through the measurement of double-layer capacitance, charge-storage capacity (CSC), and impedance |Z|.

## 2. EXPERIMENTAL SECTION

**2.1. Diamond Growth.** A homogeneous polycrystalline boron-doped diamond film (4 $\mu$m thick) was grown in a hot-filament CVD (HFCVD) reactor ($sp^3$ Diamond Technologies) on an 8″ Si wafer, following a seeding procedure described elsewhere.[32] The growth conditions consisted of 8 mbar atmosphere, 2.4% $CH_4/H_2$ gas ratio (72 sccm/3000 sccm), 40 sccm trimethylborane (TMB), and ∼850 °C temperature. The achieved B-doping level was ∼2.8 atom %, as measured from secondary ion mass spectrometry (SIMS), and the BDD film resistivity was $\sim 5 \times 10^{-3}$ Ω cm.[33] Identical samples were produced by dicing the grown wafer into neighboring pieces of ∼1.5 × 1.5 $cm^2$.

**2.2. Laser Texturing.** The LIPSS process was achieved with a femtosecond laser of 800 nm wavelength, linearly polarized, focused perpendicularly onto the BDD sample surface (spot size, ⌀160 $\mu$m; ablation size, ∼⌀100 $\mu$m). The samples were processed in a high-vacuum chamber ($<2 \times 10^{-6}$ mbar), placed onto an $X-Y$ stage for the control of the raster movement (i.e., laser path). By controlling the raster speed, the laser accumulated fluence, which is defined as the energy of a single pulse multiplied by the number of pulses impinging at a given point on the sample surface, was defined. The vertical step between each horizontal raster line was set at 100 $\mu$m, to align the ablated zones. The laser pulse energy was kept constant at 0.65 mJ, thus corresponding to a fluence of 3.25 J/$cm^2$, which is above the diamond ablation threshold of 0.3 J/$cm^2$.[34] More details about the setup can be found in the Supporting Information.

**2.3. Structure and Morphology Characterization.** Raman spectroscopy measurements were performed with a Horiba LabRAM HR setup, equipped with an argon ion laser operating at 514 nm and a spectral resolution of ∼0.3 $cm^{-1}$. High-resolution scanning electron microscopy (FE-SEM) measurements were performed with a field emission FEI Nova NanoSEM 450 setup operating at 15 keV, with a high-resolution (immersion mode) secondary electron detector.

**2.4. Surface Characterization.** Contact angle measurements of the BDD samples were performed with an Attension Theta setup from Biolin Scientific, at ambient conditions. The droplet size was 3 $\mu$L of deionized water. XPS data were collected using a PHI5600 photoelectron spectrometer (Physical Electronics) with an Al K$\alpha$ monochromatic X-ray source (1486.71 eV energy). Measurements were done before and after sputtering with $Ar^+$ to remove contamination. The XPS data were analyzed with PHI MultiPak software without binding energy correction, due to the high conductivity of the samples. More details can be found in the Supporting Information.

**2.5. Electrochemical Characterization.** Solutions containing 1 mM concentration of either ferrocyanide or hexaammineruthenium-(III) chloride (RuHex) in a 0.1 M KCl aqueous solution were employed for electrochemical characterization. The laser-textured BDD samples were analyzed (1) after texturing, (2) after cleaning in boiling concentrated acid, and (3) after strong polarization in nitric acid. A glassy carbon (GC) electrode was also used for comparison. Before acid cleaning, the samples were consecutively ultrasonicated in acetone, ethanol, and DI water to remove any loose debris formed by the laser-texturing process.

The electrochemical measurements were performed by a multichannel Metrohm Autolab potentiostat/galvanostat setup, equipped with an 8 × M101 channel and a 1 × FRA2M impedance analysis module. Cyclic voltammetry (CV) and electrochemical impedance


DOI: 10.1021/acsami.8b15951
ACS Appl. Mater. Interfaces 2018, 10, 43236−43251

spectroscopy (EIS) measurements were done in a three-electrode configuration, with a Ag/AgCl reference electrode and a working electrode area $A$ = 0.219 $cm^2$. More details about the electrochemical cell can be found in the Supporting Information. Electric contact to the sample surface was achieved with conductive silver paint. The CV data were treated and analyzed with the Nova software (Metrohm) and a MATLAB script developed in-house.

EIS measurements were done with a 10 mV RMS perturbation signal and a frequency range of $10^{-1}$–$10^{5}$ Hz. In the presence of analyte, an offset potential equal to the formal potential, $V_0$, was applied. The measured data were fitted to the Randles circuit in two steps, using the Nova software and the MATLAB ZfitGUI script (available online at the File Exchange portal from MATLAB central).

**2.6. Chemicals.** Hexaammineruthenium(III) chloride ($Ru(NH_3)_6Cl_3$, 98%) and potassium hexacyanoferrate(II) trihydrate ($K_4Fe(CN)_6{\cdot}3H_2O$, >99%) were obtained from Sigma-Aldrich and used as redox mediators without further purification. The supporting electrolyte for $Ru(NH_3)_6^{3+/2+}$ and $Fe(CN)_6^{4-/3-}$ consisted of 0.1 M potassium chloride (KCl from Sigma-Aldrich, ≥99%). All of the solutions were prepared with ∼18 MΩ cm, Type I water (ELGA Purelab UHQ) and bubbled with $N_2$ to remove dissolved $O_2$ before each measurement. Acid cleaning of the samples was done in a boiling mixture of HCl (38%), $H_2SO_4$ (95%), and $HNO_3$ (70%) (1:1:1 volume ratio), followed by thorough ultrasonication in deionized water.

## 3. RESULTS

**3.1. Laser Texturing.** Optimum conditions for laser texturing of the 4 μm thick, heavily doped BDD were found after a systematic survey of parameters was carried out on a test BDD sample, by changing the laser pulse energy, the number of repetitions, and the raster speed, $v_r$. Starting at 3.35 mJ/pulse (50 pulses and $v_r$ = 0 mm/s), there was significant damage of the film at the central area of the laser spot (ca. ⌀40 μm inside the ⌀100 μm ablation spot), which decreased as the energy was lowered down to 0.65 mJ/pulse. This lowest energy produced the best outcome, showing consistent formation of quasi-periodic structures across the whole laser spot. We also observed that, even for this low energy value, increasing the number of pulses to ∼100 led to the destruction of the diamond film. Taking these parameters into consideration, a range of conditions for the laser texturing of our BDD samples were established (see Table S1 in the Supporting Information), with ripples being observed from 14 to 410 J/$cm^2$ (see Figure S1). Out of the total seven samples produced within that accumulated fluence range, two distinct ones were taken for in-depth comparison: BDD-42 with low accumulated fluence and BDD-500 with high accumulated fluence (see Table 1).

**Table 1. Summary of Parameters Used for Laser-Textured Samples BDD-42 and BDD-500 (Low and High Accumulated Fluences, Respectively)**

| parameter | BDD-42 | BDD-500 |
|---|---|---|
| $v_r$ (mm/s) | 2.25 | 1.88 |
| pulse repetition rate (Hz) | 100 | 1000 |
| pulses per unit treated area ($cm^{-2}$) | $42 \times 10^3$ | $500 \times 10^3$ |
| accumulated fluence (J/$cm^2$) | 27 | 325 |

SEM and Raman analyses of the laser-textured samples were carried out before cleaning or any chemical treatment and are shown in Figures 1 and 2, respectively. Measurements of a reference untreated BDD are also included for comparison.

It can be seen from the SEM images that the laser texturing produced significant morphological changes to the BDD surface. While before the treatment the individual crystallites and grain boundaries of the BDD films can be clearly seen (Figure 1a,d), after texturing, the surfaces consist entirely of quasi-periodic, elongated structures aligned preferentially perpendicular to the laser polarization direction and perpendicular to the raster direction. The low accumulated fluence treatment (Figure 1b,e) shows the formation of ripples ∼165 nm wide, as well as the presence of "faults" (marked with dashed elippses), where adjacent ripples are merged together as a single, larger structure. The surface modified by the high accumulated fluence treatment (Figure 1c,f) is characterized by ripples that are straighter, narrower (∼125 nm wide), and more clearly separated from one another, thus achieving better morphology. These structures resemble those obtained under similar conditions in a previous work,[25] where the ripple periodicity is explained as the outcome of the interference between surface plasmons and the incident laser, which gives a nominal average periodicity of $\lambda/2n$ = 167 nm (where $\lambda$ = 800 nm is the wavelength of the laser and $n$ = 2.4 is the refractive index of diamond at 800 nm). The higher level of imperfection of the ripples observed in the present work can be attributed to the more irregular topography of the as-grown BDD, with coexistence of micro- and nanosized crystalline facets at the film surface, which is inherent to the CVD growth process, as can be seen in Figure 1a,d. Additionally, the improved morphology of BDD-500 relative to BDD-42 is coherent with the observation that, for subwavelength periodicity LIPSS process, the spatial periodicity on the surface decreases with increasing number of pulses.[20]

The reference BDD displays a typical Raman spectrum (Figure 2a) of a heavily B-doped diamond film, with strong distortion of the diamond one-phonon line (1332 $cm^{-1}$) into two separate branches located at 1200–1300 $cm^{-1}$, due to the Fano resonance effect.[35] Simultaneously, the ∼454 $cm^{-1}$ broad band, which is attributed to Raman scattering involving B–C vibrational modes,[36] is visible. The G-band is also visible, likely arising from graphitic material present in the grain boundaries of the BDD film. On the other hand, the spectra of the laser-textured samples show predominantly the D- and G-bands, which originate from $sp^2$ carbon present in both disordered/defective and crystalline forms of graphite.[37,38]

To remove debris and redeposited material from the LIPSS process, as well as to have a more stable oxygenated surface, the laser-textured samples (Figure 2b,d) were subjected to acid cleaning in a strong, highly oxidizing bath containing HCl (38%), $H_2SO_4$ (95%), and $HNO_3$ (70%) (1:1:1 volume ratio). Raman and SEM measurements after the cleaning are shown, respectively, in Figure 2a and Figure 2c,e, and compared to the results before the procedure. It can be seen that the D- and G-bands in the Raman spectra became narrower, indicating higher material quality, but lower intensity relative to the B–C band from the BDD underneath, which indicates decreased thickness of this $sp^2$ carbon layer. At the same time, the SEM images show narrower ripples and larger gaps between them, thus suggesting that disordered carbon from the immediate surface was removed by the acid cleaning. As it can be seen in more detail in Figure S2 (Supporting Information), no obvious trend in the Raman spectra as a function of laser fluence was found, neither before nor after acid cleaning. We attribute this to a complex behavior of material melting, ejection, and redeposition onto the surface during the different laser-texturing conditions, which affect the composition of the surface in addition to the LIPSS pattern itself.


DOI: 10.1021/acsami.8b15951
ACS Appl. Mater. Interfaces 2018, 10, 43236–43251

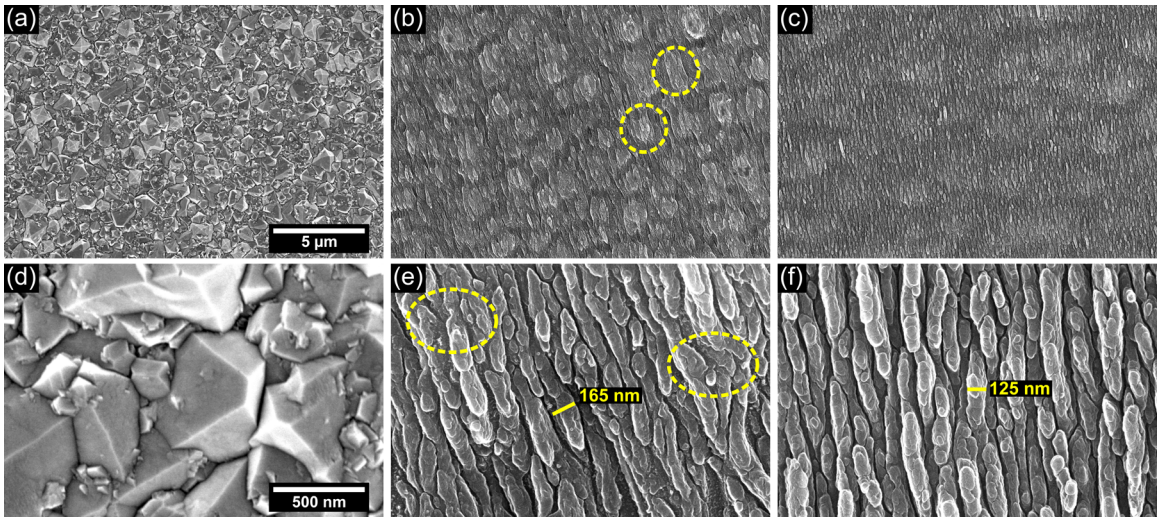


**Figure 1.** SEM images of (a, d) reference (untreated) BDD, (b, e) laser-textured sample BDD-42 (low accumulated fluence), and (c, f) laser-textured sample BDD-500 (high accumulated fluence). Top images (a–c): low magnification ($\times 10^4$), same scale; bottom images (d–f): high magnification ($\times 10^5$), same scale. The solid lines in (e, f) indicate approximate width values of the ripples; the dashed ellipses in (b, e) indicate faults in the periodicity of the ripples.

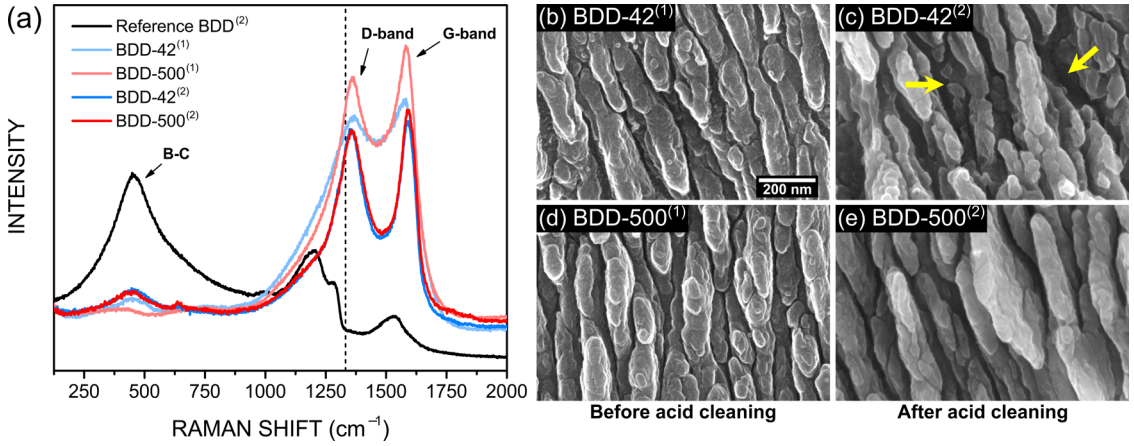


**Figure 2.** (a) Raman spectra of the laser-textured samples BDD-42 (low accumulated fluence) and BDD-500 (high accumulated fluence) before (1) and after (2) acid cleaning. The spectrum of the acid-cleaned reference BDD is also included for comparison. The as-measured curves were normalized relative to the background around 70 $cm^{-1}$. The dashed vertical line indicates the position of the (undoped) diamond one-phonon Raman line. (b–e) SEM images of laser-textured samples before (b, d) and after (c, e) acid cleaning, showing clear loss of material. (b,c) Low-fluence BDD-42, (d,e) high-fluence BDD-500. The arrows indicate clear signs of chemical etching.

Overall, the high $sp^2$ carbon content on the surface suggests that the LIPSS process induces stronger graphitization of the heavily B-doped diamond than of diamond with lower B-doping levels, as will be discussed in Section 4.1.

**3.2. Cyclic Voltammetry.** In a first step, the potential window and the background current of the laser-textured samples were measured by cyclic voltammetry in 0.1 M KCl. The voltammograms measured (1) before and (2) after acid cleaning are shown, respectively, in Figure S3 (Supporting Information) and Figure 3. The results were compared to the same measurements performed on the reference BDD in the acid-cleaned state (2), which has a stable oxygenated surface and therefore more reproducible electrochemical behavior. The increased hydrophilicity confirms the oxygenation of the surface, as shown by contact angle measurements (Figure S4 in the Supporting Information). Before acid cleaning (Figure S3), the voltammograms of both laser-textured samples displayed identical potential windows of ~2.1 V and comparable background current values of 19–20 $\mu A/cm^2$ (i.e., 190–200 $\mu F/cm^2$). In contrast, the reference BDD sample showed a larger potential window of ~2.4 V and a much lower background current of ~2 $\mu A/cm^2$ (i.e., ~20 $\mu F/cm^2$). However, after acid cleaning (Figure 3), the two laser-textured samples showed quite distinct behaviors: although the voltammogram of BDD-42 (low accumulated fluence) remained effectively unchanged, the background current of BDD-500 (high accumulated fluence) more than tripled to a value of ~66 $\mu A/cm^2$ (i.e., ~660 $\mu F/cm^2$). In fact, we observed a general linear trend of increasing capacitance for increasing laser accumulated fluence, but the scatter was high (i.e., $r^2 = 0.38$). The sample treated with the highest fluence of 410 $J/cm^2$ resulted in ~108 $\mu A/cm^2$ (i.e., ~1080 $\mu F/cm^2$). In comparison, a reference glassy carbon (GC) electrode resulted in a much lower value of ~7.6 $\mu A/cm^2$ (i.e., ~76 $\mu F/cm^2$). Overall, the voltammograms of the laser-textured samples resemble the voltammograms of glassy carbon electrodes,[10,39]


DOI: 10.1021/acsami.8b15951
ACS Appl. Mater. Interfaces 2018, 10, 43236–43251

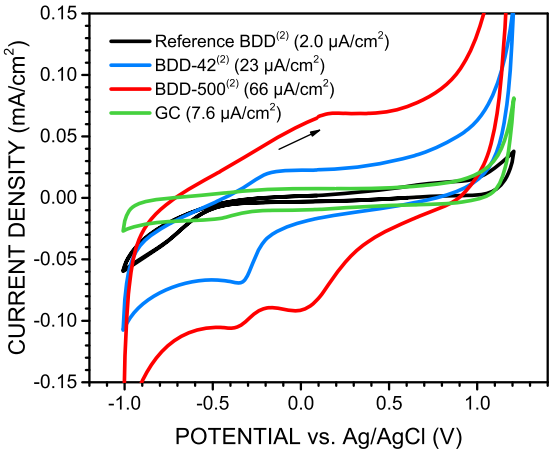


**Figure 3.** Cyclic voltammograms of laser-textured samples BDD-42 (low accumulated fluence), BDD-500 (high accumulated fluence), and reference BDD, all (2) after acid cleaning, measured in 0.1 M KCl aqueous solution at 0.1 V/s scan rate. Measurement with a glassy carbon (GC) electrode was added for comparison. Each curve corresponds to the 10th cycle. The indicated background current values were measured at 0.1 V during the forward scan.

which typically show a narrower potential window and larger background current than BDD electrodes. The reduction current onset observed at around −0.3 V for both samples arises likely from $sp^2$-catalyzed reduction of functional groups present at the surface. The additional peak at ∼0 V observed only for BDD-500 and the concomitant appearance of an oxidation peak at ∼0.2 V might be related to the redox reaction of functional groups only present at this electrode and explain in part its larger background current.

*3.2.1. Ferrocyanide.* Next, 1 mM ferrocyanide was added to the 0.1 M KCl buffer solution, and the laser-textured samples were analyzed by cyclic voltammetry performed at different scan rates. Measurements were done (1) before and (2) after acid cleaning, and the results are shown in Figure S5 (Supporting Information) and Figure 4, respectively. The plots are presented without correction for the potential drop, $iR_S$, induced by bulk resistances. Overall, all three samples showed qualitatively similar results, with comparable anodic and cathodic peak positions ($V_{P,A}$ in the range of ca. 0.2−0.3 V) and peak currents ($J_{P,A}$ in the range of ∼0.2 mA/cm$^2$ at 0.1 V/s). The higher capacitive charging of the laser-textured samples, relative to the reference BDD, is evident both before and after acid cleaning, from the large difference between anodic and cathodic currents observed between −0.5 and 0 V.

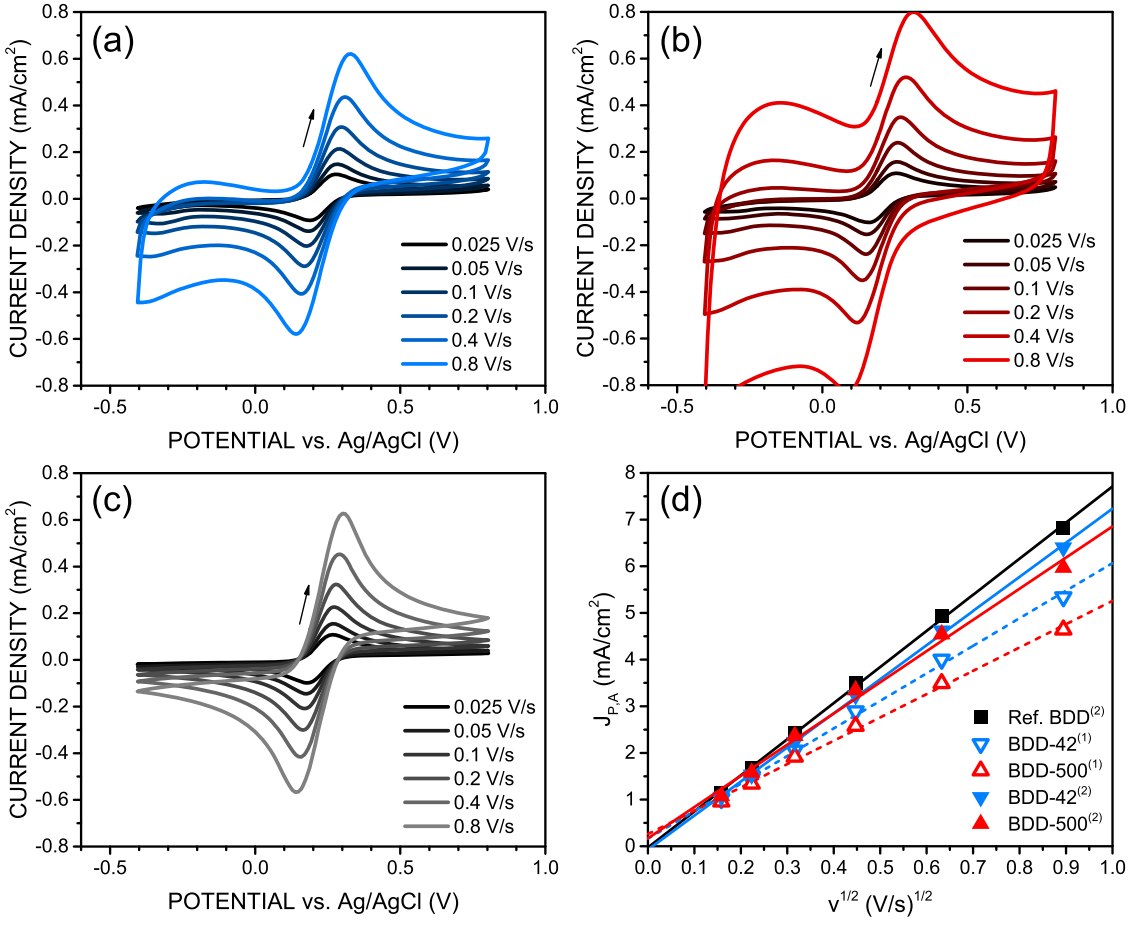


**Figure 4.** (a−c) Cyclic voltammograms of acid-cleaned samples in 0.1 M KCl aqueous solution containing 1 mM $Fe(CN)_6^{3-/4-}$ at different scan rates. (a) Low accumulated fluence sample BDD-42, (b) high accumulated fluence sample BDD-500, and (c) reference BDD sample. Each CV curve corresponds to the 10th cycle. (d) Relationship between anodic peak current density and square root of the scan rate for each sample. The open symbols with dashed lines belong to measurements (1) before acid cleaning; the closed symbols with full lines correspond to measurements (2) after acid cleaning. The adjusted coefficients of determination, $r^2$, of the linear fits were all above 0.993.



DOI: 10.1021/acsami.8b15951
ACS Appl. Mater. Interfaces 2018, 10, 43236−43251

**Table 2. Summary of the Electrochemical Parameters Obtained by CV (at 0.1 V/s) and EIS (at the Formal Potential) of All Samples in 0.1 M KCl Solution with 1 mM $Fe(CN)_6^{3-/4-}$**[a]

| | ref BDD | BDD-42 (low fluence) | | | BDD-500 (high fluence) | | |
|---|---|---|---|---|---|---|---|
| sample | (2) | (1) | (2) | (3) | (1) | (2) | (3) |
| **Cyclic voltammetry ($iR_S$-compensated)** | | | | | | | |
| $J_{P,A}$ ($\mu$A/cm$^2$) | 243.12 ± 0.21 | 205.01 ± 0.15 | 223.15 ± 0.17 | 232.51 ± 0.22 | 191.37 ± 0.14 | 236.42 ± 0.18 | 233.21 ± 0.23 |
| $V_{P,A}$ (mV) | 264.3 ± 2.5 | 284.2 ± 2.5 | 280.4 ± 2.5 | 235.2 ± 2.5 | 277.9 ± 2.5 | 250.2 ± 2.5 | 237.7 ± 2.5 |
| $\Delta V_P$ (mV) | 85.4 ± 3.5 | 113.2 ± 3.6 | 95.2 ± 3.6 | 77.4 ± 3.5 | 138.5 ± 3.6 | 90.5 ± 3.6 | 77.1 ± 3.6 |
| $V_0$ (mV) | 221.6 ± 1.8 | 227.6 ± 1.8 | 232.8 ± 1.8 | 196.4 ± 1.8 | 208.6 ± 1.8 | 205.0 ± 1.8 | 199.1 ± 1.8 |
| $D \times 10^8$ (cm$^2$/s) | 828 ± 47 | 483 ± 35 | 738 ± 41 | 873 ± 44 | 345 ± 27 | 615 ± 61 | 880 ± 44 |
| $k_0$ ($\mu$m/s) | 96 ± 14 | 35.2 ± 2.7 | 65.7 ± 6.8 | 143 ± 29 | 20.2 ± 1.2 | 69.1 ± 8.7 | 147 ± 31 |
| $\Lambda = k_0(RT/FDv)^{1/2}$ | 1.68 ± 0.14 | 0.806 ± 0.038 | 1.216 ± 0.074 | 2.44 ± 0.28 | 0.547 ± 0.022 | 1.40 ± 0.11 | 2.48 ± 0.29 |
| **Electrochemical impedance spectroscopy** | | | | | | | |
| $R_S$ ($\Omega$) | 182 | 188 | 186 | 188 | 182 | 193 | 191 |
| $R_{CT}$ ($\Omega$) | 133 | 591 | 309 | 44 | 969 | 449 | 32 |
| $Q_0 \times 10^5$ ($s^n/\Omega$) | 0.35 | 4.99 | 4.96 | 3.75 | 2.72 | 11.11 | 2.46 |
| $n_Q$ | 0.93 | 0.87 | 0.87 | 0.76 | 0.89 | 0.89 | 0.83 |
| $C_{dl\ eq.}$ ($\mu$F/cm$^2$) | 10 | 175 | 159 | 38 | 99 | 432 | 36 |
| $W_0 \times 10^5$ ($s^{1/2}/\Omega$) | 69.3 | 62.2 | 61.1 | 51.1 | 58.1 | 61.0 | 54.4 |
| $n_W$ | 0.52 | 0.53 | 0.52 | 0.50 | 0.50 | 0.52 | 0.50 |
| $\chi^2 \times 10^4$ | 9 | 39.5 | 4.7 | 33.3 | 96 | 8.1 | 21.3 |

[a]The numbers (1−3) stand for the different sample states: (1) not acid-cleaned; (2) acid-cleaned; and (3) after strong polarization in $HNO_3$.

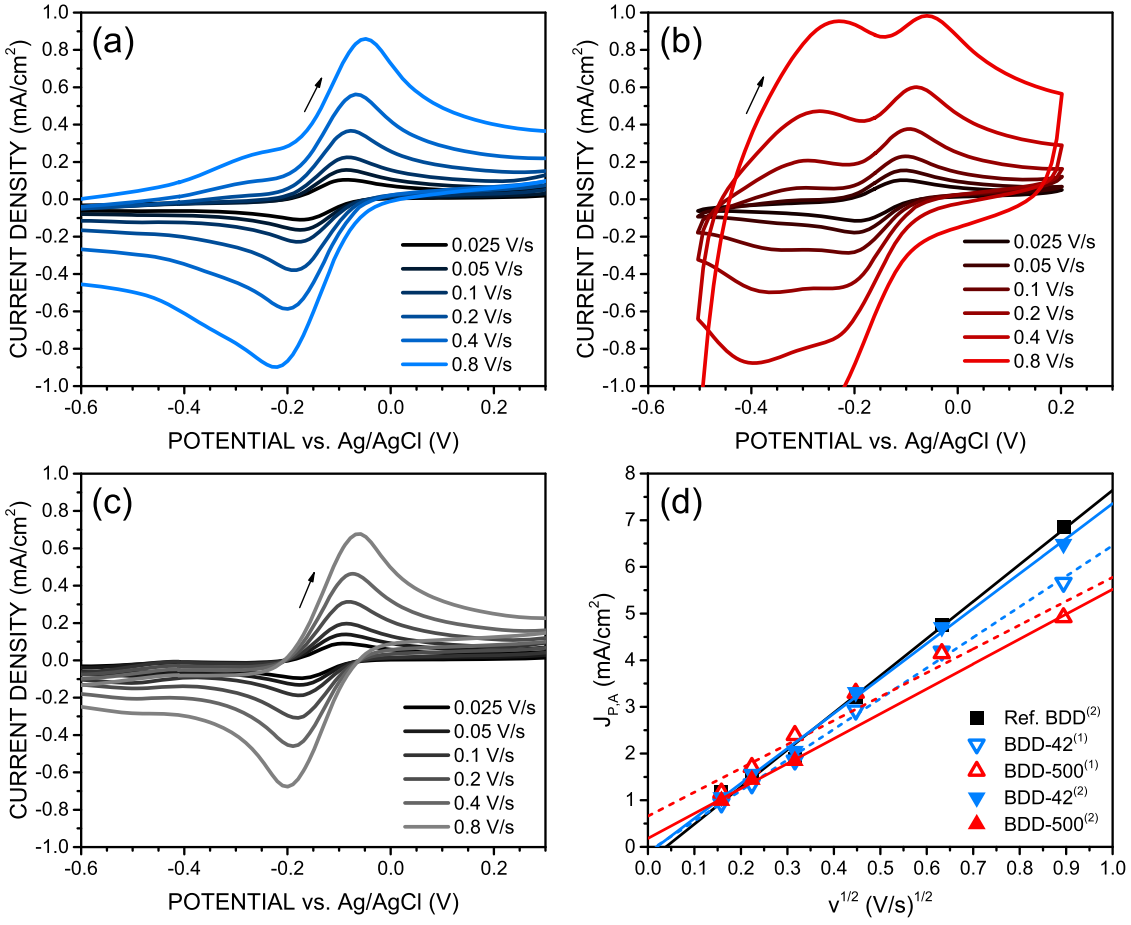


**Figure 5.** (a−c) Cyclic voltammograms of acid-cleaned samples in 0.1 M KCl aqueous solution containing 1 mM $Ru(NH_3)_6^{3+/2+}$ at different scan rates. (a) Low accumulated fluence sample BDD-42, (b) high accumulated fluence sample BDD-500, and (c) reference BDD sample. Each CV curve corresponds to the 10th cycle. (d) Relationship between anodic peak current density and square root of the scan rate for each sample. The open symbols with dashed lines denote measurements (1) before acid cleaning; the closed symbols with full lines correspond to measurements (2) after acid cleaning. The adjusted $r^2$ values of the linear fits were all above 0.95.



DOI: 10.1021/acsami.8b15951
ACS Appl. Mater. Interfaces 2018, 10, 43236−43251

Table 3. Summary of the Electrochemical Parameters Obtained by CV (at 0.1 V/s) and EIS (at the Formal Potential) of All Samples, Measured in 0.1 M KCl Solution with 1 mM $Ru(NH)_6^{3+/2+}$[a]

| | ref BDD | BDD-42 (low fluence) | | | BDD-500 (high fluence) | | |
|---|---|---|---|---|---|---|---|
| sample | (2) | (1) | (2) | (3) | (1) | (2) | (3) |
| **Cyclic voltammetry ($iR_S$-compensated)** | | | | | | | |
| $J_{P,A}$ ($\mu$A/cm$^2$) | 188.86 ± 0.39 | 184.96 ± 0.35 | 205.83 ± 0.39 | 245.53 ± 0.44 | 240.17 ± 0.52 | 184.24 ± 0.28 | 238.61 ± 0.45 |
| $V_{P,A}$ (mV) | −93.3 ± 2.5 | −101.5 ± 2.5 | −91.2 ± 2.5 | −117.7 ± 2.5 | −112.4 ± 2.5 | −110.4 ± 2.5 | −117.9 ± 2.5 |
| $\Delta V_P$ (mV) | 76.3 ± 3.6 | 78.1 ± 3.5 | 79.1 ± 3.6 | 77.2 ± 3.5 | 78.2 ± 3.6 | 91.3 ± 3.6 | 77.3 ± 3.5 |
| $V_0$ (mV) | −131.5 ± 1.8 | −140.5 ± 1.8 | −130.8 ± 1.8 | −156.3 ± 1.8 | −151.5 ± 1.8 | −156.1 ± 1.8 | −156.6 ± 1.8 |
| $D \times 10^8$ (cm$^2$/s) | 877 ± 83 | 598 ± 45 | 778 ± 55 | 984 ± 52 | 364 ± 75 | (39 ± 11)× 10$^1$ | 908 ± 49 |
| $k_0$ ($\mu$m/s) | 154 ± 34 | 114 ± 22 | 123 ± 23 | 154 ± 32 | 89 ± 19 | 53.9 ± 9.6 | 147 ± 30 |
| $\Lambda = k_0(RT/FDv)^{1/2}$ | 2.61 ± 0.33 | 2.35 ± 0.26 | 2.22 ± 0.24 | 2.47 ± 0.29 | 2.33 ± 0.32 | 1.36 ± 0.17 | 2.45 ± 0.28 |
| **Electrochemical impedance spectroscopy** | | | | | | | |
| $R_S$ (Ω) | 188 | 189 | 183 | 187 | 178 | 192 | 192 |
| $R_{CT}$ (Ω) | 60 | 22 | 9.4 | 27 | 58 | 13 | 28 |
| $Q_0 \times 10^5$ ($s^n$/Ω) | 17 | 8.8 | 4.11 | 3.57 | 12.3 | 25.6 | 3.4 |
| $n_Q$ | 0.67 | 0.86 | 0.95 | 0.83 | 0.80 | 0.81 | 0.84 |
| $C_{dl\ eq.}$ ($\mu$F/cm$^2$) | 175 | 188 | 139 | 56 | 240 | 447 | 57 |
| $W_0 \times 10^5$ ($s^{1/2}$/Ω) | 60.3 | 65.4 | 75.0 | 56.9 | 58.3 | 51.0 | 56.2 |
| $n_W$ | 0.49 | 0.52 | 0.54 | 0.50 | 0.49 | 0.46 | 0.50 |
| $\chi^2 \times 10^4$ | 5.9 | 8.7 | 35.6 | 28.8 | 7.2 | 6.8 | 22.2 |

[a]The numbers (1−3) stand for the different sample states: (1) not acid-cleaned; (2) acid-cleaned; and (3) after strong polarization in $HNO_3$.

BDD-500 showed again substantially higher capacitive charging than BDD-42 after acid cleaning. The narrower potential window of the laser-textured samples, in comparison to reference BDD, is also visible, as the current density increases at the extremities of the voltammograms (i.e., onset of hydrolysis current). The obtained peak−peak separations, $\Delta V_P$ = 90−95 mV, and anodic peak current densities, $J_{P,A}$ = 0.223−0.236 mA/cm$^2$, in ferrocyanide are in the range expected for BDD and GC.[40]

A more detailed analysis of electrode kinetics for ferrocyanide was carried out as follows. For each sample, several voltammograms were measured at different scan rates, $v$, ranging from 0.025 to 0.8 V/s. The voltammograms were then corrected for the $iR_S$ potential drop, with the series resistances, $R_S$, obtained from EIS (see section 3.3). Then, according to the Randles−Sevčik equation,[41] the background-corrected peak current density, $J_{P,A}$, was plotted against the square root of the scan rate, $v^{1/2}$, for each electrode, as shown in Figure 4d, and fitted to a first-degree polynomial. The diffusion coefficient, $D$, of electroactive species near the electrode surface was obtained from the slope, assuming the area $A$ as the known geometric surface area. The electron-transfer rate, $k_0$, of each electrode was estimated from the well-known Nicholson method.[42] This method assumes quasi-reversible kinetics and relates $k_0$ directly to the ($iR_S$-corrected) peak−peak potential, $\Delta V_P$. All parameters obtained for $v$ = 0.1 V/s are summarized in Table 2.

The linearity of $J_{P,A}$ as a function of $v^{1/2}$ in Figure 4d can be seen for all electrodes, which is characteristic of diffusion-controlled (i.e., mass transport-limited) kinetics and fast heterogeneous electron transfer. The $iR_S$-corrected peak−peak separation increased only slightly with increasing scan rate, indicating quasi-reversible behavior for all electrodes. The figure of merit[41] $\Lambda = k_0(RT/FDv)^{1/2}$ calculated for each scan rate also pointed to quasi-reversible kinetics, as $15 \geq \Lambda \geq 10^{-3}$ (assuming the transfer coefficient $\alpha$ = 0.5). As shown in Table 2 for $v$ = 0.1 V/s, the reference BDD (acid-cleaned) had the highest $k_0$ of 96 $\mu$m/s among all acid-cleaned samples. The laser-textured samples attained a higher electron-transfer rate after acid cleaning, with $k_0$ = 69 and 66 $\mu$m/s for BDD-500 (high fluence) and BDD-42 (low fluence), respectively. The reference BDD showed the highest diffusion coefficient value of $D$ = 828 $\mu$m$^2$/s, whereas BDD-42 showed $D$ = 483 $\mu$m$^2$/s before acid cleaning and $D$ = 738 $\mu$m$^2$/s after acid cleaning. BDD-500 improved from $D$ = 345 to 615 $\mu$m$^2$/s. It must be noted, however, that the laser-texturing process most likely increased the surface area of the electrodes with the creation of nanoripples, and thus the obtained diffusion coefficients for BDD-42 and BDD-500 are likely overestimated. The fact that $D$ increased after acid cleaning is consistent with an increase in surface area, and the overall lower values compared to the reference BDD are consistent with the hindering of mass transport to and from the electrode surface due to porosity. The reference BDD also yielded better figures for the anodic peak current density, $J_{P,A}$, and the peak−peak separation, $\Delta V_P$, whereas the laser-textured samples showed improvement after acid cleaning and similar performance. The combined results point to faster kinetics for the reduction and oxidation of ferrocyanide on the reference BDD and highlight the positive effect of acid cleaning on the electrochemical performance of the laser-textured BDD.

*3.2.2. RuHex.* The same analysis was subsequently done in RuHex, with the results (1) before and (2) after acid cleaning shown, respectively, in Figure S6 and Figure 5. A summary of the obtained parameters is shown in Table 3. Overall, after $iR_S$ correction, the peak−peak separation was found to be almost independent of the scan rate, showing quasi-reversible kinetics for all electrodes, as also indicated by the figure of merit Λ. Before acid cleaning, BDD-42 (low accumulated fluence) showed faster kinetics than BDD-500 (high accumulated fluence), but slower kinetics than the reference BDD. The values for the diffusion coefficient and electron-transfer rate of the latter sample resulted in, respectively, $D$ = 877 $\mu$m$^2$/s and $k_0$ = 154 $\mu$m/s. For BDD-42, the diffusion coefficient increased from $D$ = 598 to 778 $\mu$m$^2$/s and $k_0$ remained effectively constant at 114−123 $\mu$m/s after acid cleaning. For BDD-500, the diffusion coefficient increased marginally from $D$ = 364 to 390 $\mu$m$^2$/s, whereas $k_0$ decreased from 89 to 54 $\mu$m/s after acid


DOI: 10.1021/acsami.8b15951
ACS Appl. Mater. Interfaces 2018, 10, 43236−43251

cleaning. Much higher background currents were again observed for BDD-500 after acid cleaning to such an extent that it interfered with the fitting of the voltammograms for higher scan rates (see Figure 5d): before acid cleaning, the $J_{P,A}$ vs $v^{1/2}$ relationship is arguably nonlinear, whereas the curve measured after acid cleaning, although apparently linear, lacks the values for higher scan rates. This led to uncertainty in the calculated slopes, which affected the diffusion coefficient, $D$, and thus also $k_0$ and $\Lambda$. Consequently, it is not possible to affirm an improvement of this electrode's kinetics after acid cleaning, despite this being the expected outcome. The much higher background current of BDD-500 between −0.4 and −0.3 V after acid cleaning (Figure 5) appears to be related to an additional redox process occurring at the surface of the electrode, as suggested by the shape of the voltammograms with extra reduction and oxidation waves in that potential region. Overall, the results with RuHex point to practically similar kinetics among the reference BDD and the laser-textured samples, with the main difference being the increased background current of the high-fluence BDD-500. The obtained peak−peak potentials, $\Delta V_P$ = ∼80 mV, and anodic peak current densities, $J_{P,A}$ = ∼0.2 mA/cm$^2$, are in the range expected for BDD and GC.[40,43]

**3.3. Electrochemical Impedance Spectroscopy.** To better support the results from cyclic voltammetry, impedance spectroscopy was employed. Measurements were done in a 0.1 M KCl buffer solution, with and without analyte (i.e., 1 mM ferrocyanide or RuHex); the impedance data were fitted to the Randles circuit[44] shown in Figure 6, and the final obtained

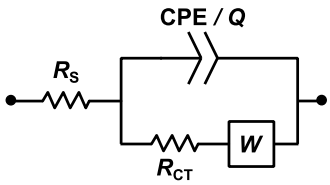


**Figure 6.** Randles circuit modeling a single faradic reaction coupled with mass transfer. It contains the electric double layer in the constant-phase element (CPE), $Q$, the heterogeneous electron transfer in $R_{CT}$, and the diffusion of species near the electrode surface in the Warburg element, $W$. In the fitting, $W$ was treated as a CPE with a phase of ∼45° (i.e., $n_W$ ≈0.5). The series resistance, $R_S$, accounts for bulk electrode resistivity, electrolyte resistivity, and contact resistances.

parameters are listed in Tables 2 and 3, respectively, for ferrocyanide and RuHex. The $\chi^2$ values (sum of weighted squares of residuals) indicate the high fit accuracy.

Overall, $R_S$ was consistent among all samples and solutions, with an average value of 186.1 ± 4.5 Ω. That is expected, since the base electrode material is the same, and the solutions have the same electrolyte concentration. Thus, the similar series resistance values point to the laser-textured surfaces being highly electrically conductive, with the high resistance coming from the bulk electrolyte. The charge-transfer resistance is a direct measure of electron-transfer kinetics on the electrode and can be directly related to the electron-transfer rate, i.e., $k_0 \propto 1/R_{CT}$.[45] In ferrocyanide, both BDD-42 (low accumulated fluence) and BDD-500 (high accumulated fluence) samples yielded $R_{CT}$ values which are coherent with the estimated electron-transfer rates from cyclic voltammetry. That is, the reference BDD showed the lowest $R_{CT}$ (highest $k_0$), whereas acid cleaning the laser-textured samples led to the decrease of $R_{CT}$ (thus increase of $k_0$), i.e., improved kinetics, compared to the as-laser-treated samples. In the case of RuHex, the charge-transfer resistance of both laser-textured samples improved after acid cleaning, indicating a marginal increase of electron-transfer rate.

The double-layer capacitance, $C_{dl}$, was also estimated from the impedance data, according to the procedure described by Hsu et al.,[46] where the CPE is converted to an effective capacitance as a function of its ideality factor, $n_Q$, and the frequency, $\omega_{max}$, where the imaginary part of the complex impedance, Im($Z$), is at its maximum. The obtained values are summarized in Tables 2 and 3, respectively, for ferrocyanide and RuHex. In the case of ferrocyanide, the double-layer capacitance of the laser-textured samples was >10 times higher than that of the reference BDD, which showed the lowest value of 10 μF/cm$^2$. The effect of acid cleaning on the capacitance of the laser-textured BDD samples observed with EIS was coherent with the observations with CV (see Section 3.2): the capacitance of BDD-42 (low accumulated fluence) decreased only slightly from 175 to 159 μF/cm$^2$, whereas the capacitance of BDD-500 (high accumulated fluence) increased from 99 to 432 μF/cm$^2$. The slight decrease of $C_{dl}$ for BDD-42 (in both ferrocyanide and RuHex) after acid cleaning reflects the behavior in the cyclic voltammograms (Figures 4a and 5a compared to Figures S5b and S6b), which did not see an increase in background current. This is likely a consequence of how the particular morphology of the low-fluence sample was affected by the acid cleaning procedure, which likely decreased the surface area. In fact, a linear trend of increasing $C_{dl}$ for increasing laser accumulated fluence was observed among all samples, from BDD-42 to BDD-630, with $r^2$ = 0.55. The highest-fluence sample BDD-630 resulted in the highest capacitance of 549 μF/cm$^2$ in ferrocyanide, after acid cleaning. In the case of RuHex, BDD-42 and BDD-500 yielded, respectively, 139 and 447 μF/cm$^2$ upon acid treatment, with BDD-630 showing an even higher value of 904 μF/cm$^2$.

**3.4. XPS Analysis.** To further investigate the change in electrode kinetics and the increase in double-layer capacitance after acid cleaning, additional XPS analysis of both low-fluence and high-fluence samples was performed, as shown in Figure 7. Significant changes on the composition of the surface can be seen after acid cleaning, namely, the appearance of the ∼289 eV component, which indicates the presence of oxidation states mostly attributed to carbonyl groups, and the ∼293 eV component, which is a $\pi-\pi^*$ shake-up satellite peak arising from the delocalization of electrons in conjugated aromatic compounds,[47,48] which were not present before acid cleaning. That supports the increased degree of order of the graphitic layer observed by Raman spectroscopy, as well as the activation of the surface with chemically active sites, which contribute to the enhanced double-layer capacitance. The reference BDD also shows the presence of carbonyl groups, due to the acid cleaning process. Figure 7 also includes the XPS data of BDD-42 and BDD-500 after the ripples were removed by (3) polarization in $HNO_3$, which exposed the laser-ablated diamond surface, as discussed in detail below. Figure S7 in the Supporting Information shows that contamination can be ruled out as the origin of those features in the XPS spectra.

**3.5. Effect of Polarization in Nitric Acid.** Potential cycling in nitric acid is typically performed on diamond electrodes before electrochemical measurements, to produce a more stable and electrochemically reproducible O-terminated surface.[49,50] Due to the initial interest in investigating the


DOI: 10.1021/acsami.8b15951
ACS Appl. Mater. Interfaces 2018, 10, 43236−43251

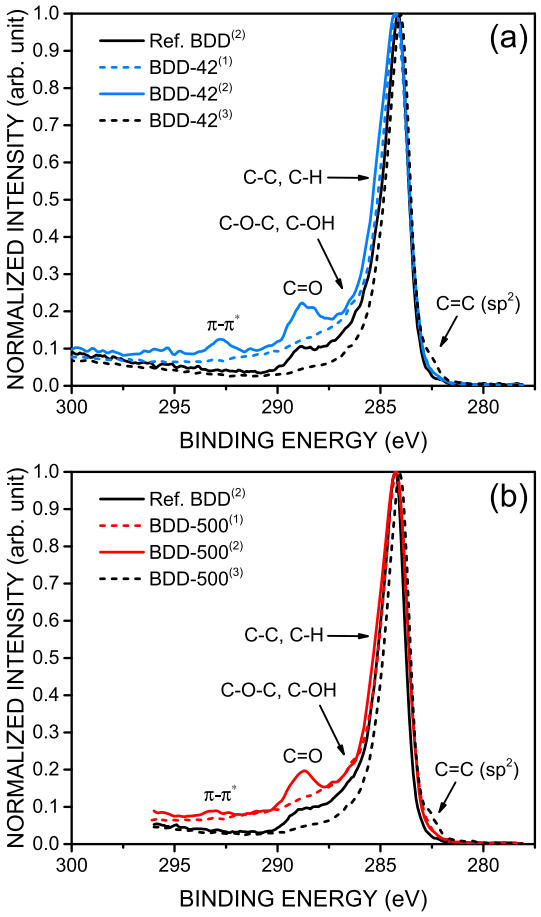


**Figure 7.** XPS spectra of the laser-textured samples at different stages: (1) before acid cleaning, (2) after acid cleaning, and (3) after polarization in $HNO_3$. (a) Low accumulated fluence sample BDD-42; (b) high accumulated fluence sample BDD-500. Spectra of the reference BDD after acid cleaning were added for comparison. The spectra are shown as measured, i.e., without correction of conductivity-induced shift in energy.

pristine laser-textured BDD surface, this procedure was skipped for the electrochemical characterization described above and applied later as a last step. A strong cycling between 2.5 and 3 V (ohmic regime) with >10 repetitions was chosen to remove the $sp^2$ carbon layer from the diamond and to quickly stabilize the electrode in an oxygenated state. After that, the samples were again measured in 0.1 M KCl with and without 1 mM ferrocyanide or RuHex. The results are shown in Figure 8 and summarized in Tables 2 and 3, respectively.

It can be seen that, after strong polarization in $HNO_3$, the background current of the laser-textured samples became much smaller than before (more than 5-fold for BDD-500), down to ~6 $\mu A/cm^2$, and much more similar to the background current of the reference BDD. Also, the potential windows became almost identical to those of the reference BDD. The drastic change in background current can also be seen in the voltammograms measured in ferrocyanide and RuHex (Figure 8a–d) compared to Figures 4 and 5. Both low- and high-fluence samples showed an identical behavior after strong polarization in $HNO_3$ and more similar $j-V$ profiles to the reference BDD. The impedance spectroscopy analysis of BDD-42 and BDD-500 also confirmed the decrease in background current from the reduction of the double-layer capacitance, $C_{dl}$, from 159 to 38 $\mu F/cm^2$ (>4-fold) for BDD-42 and from 432 to 36 $\mu F/cm^2$ for BDD-500 (>11-fold), measured in ferrocyanide. A similar outcome was observed in RuHex.

The electrode kinetics of BDD-42 and BDD-500 improved substantially after polarization in $HNO_3$. Looking at Table 2, in the case of ferrocyanide, it can be seen that reversibility, $\Lambda$, increased, the peak–peak potential decreased, the diffusion coefficient increased, and the rate constant also increased for both laser-textured samples. BDD-42 and BDD-500 showed nearly identical parameters. The EIS analysis also confirmed the improved kinetics with the reduction of the charge-transfer resistance, $R_{CT}$, from 309 to 44 Ω for BDD-42 and from 449 to 32 Ω for BDD-500, i.e., 3–4 times lower than that for the reference BDD. In the case of RuHex (Table 3), BDD-42 and BDD-500 also showed improved kinetics and reversibility after strong polarization in $HNO_3$, performing quite similar to the reference BDD. However, EIS showed an increase of $R_{CT}$, which contradicts the increase of $k_0$ as estimated from cyclic voltammetry. Nevertheless, the $R_{CT}$ values of 27 and 28 Ω for BDD-42 and BDD-500, respectively, are lower than the 60 Ω obtained for the reference BDD.

The change in electrochemical behavior of BDD-42 and BDD-500 was further studied by Raman spectroscopy and SEM performed on the active electrode areas that were subjected to strong polarization in nitric acid and the electrochemical measurements that followed. Figure 9a shows the Raman spectra of BDD-42 and BDD-500 after the treatment, revealing that the predominant $sp^2$ nature of the laser-textured surface (as seen in Figure 2) was reverted back to that of the untreated BDD. The SEM images in Figure 9b,c show the absence of ripples and the presence of scars, which likely originate from laser ablation of the BDD surface.

The enhanced electrochemical behavior of the laser-textured electrodes after strong polarization in nitric acid is not entirely clear. While the Raman spectra indicate a predominantly, if not exclusively, B-doped diamond surface, the plan-view SEM images (Figure 9b,c) indicate that some of the $sp^2$ carbon-rich materials from the laser-texturing process still remained on the surface, which may have conferred to the electrode surface a more favorable environment for the redox reaction of ferrocyanide, as the data from Table 2 indicate. In the case of RuHex, although the polarization in nitric acid improved the kinetics relative to the previous state (i.e., laser-textured surface, acid-cleaned), as observed from cyclic voltammetry, the values did not quite match those of the reference BDD. On the other hand, EIS data pointed to a slight decrease in performance (i.e., higher $R_{CT}$), which could be related to a decrease of surface conductivity from the loss of $sp^2$ carbon. Looking at the XPS spectra in Figure 7, it can be seen that the $\pi-\pi^*$ shake-up satellite peak and the C=O peak are not present after polarization in $HNO_3$, whereas a C=C ($sp^2$) shoulder is visible for both laser-textured samples. The results point to a substantial change of the surface, with only residual $sp^2$ carbon content left.

Further SEM analysis of all samples in cross section was carried out to better differentiate the surface morphologies (1) before laser texturing, (2) after laser texturing, and (3) after strong polarization in nitric acid. The images are shown in Figure 10. In Figure 10a, the typical polycrystalline structure of the as-grown BDD can be seen, with pyramids formed by the crystallographic facets of the individual diamond grains. Figure 10b shows the laser-textured BDD-42 (low accumulated fluence), while Figure 10d,e shows the laser-textured BDD-


DOI: 10.1021/acsami.8b15951
ACS Appl. Mater. Interfaces 2018, 10, 43236–43251

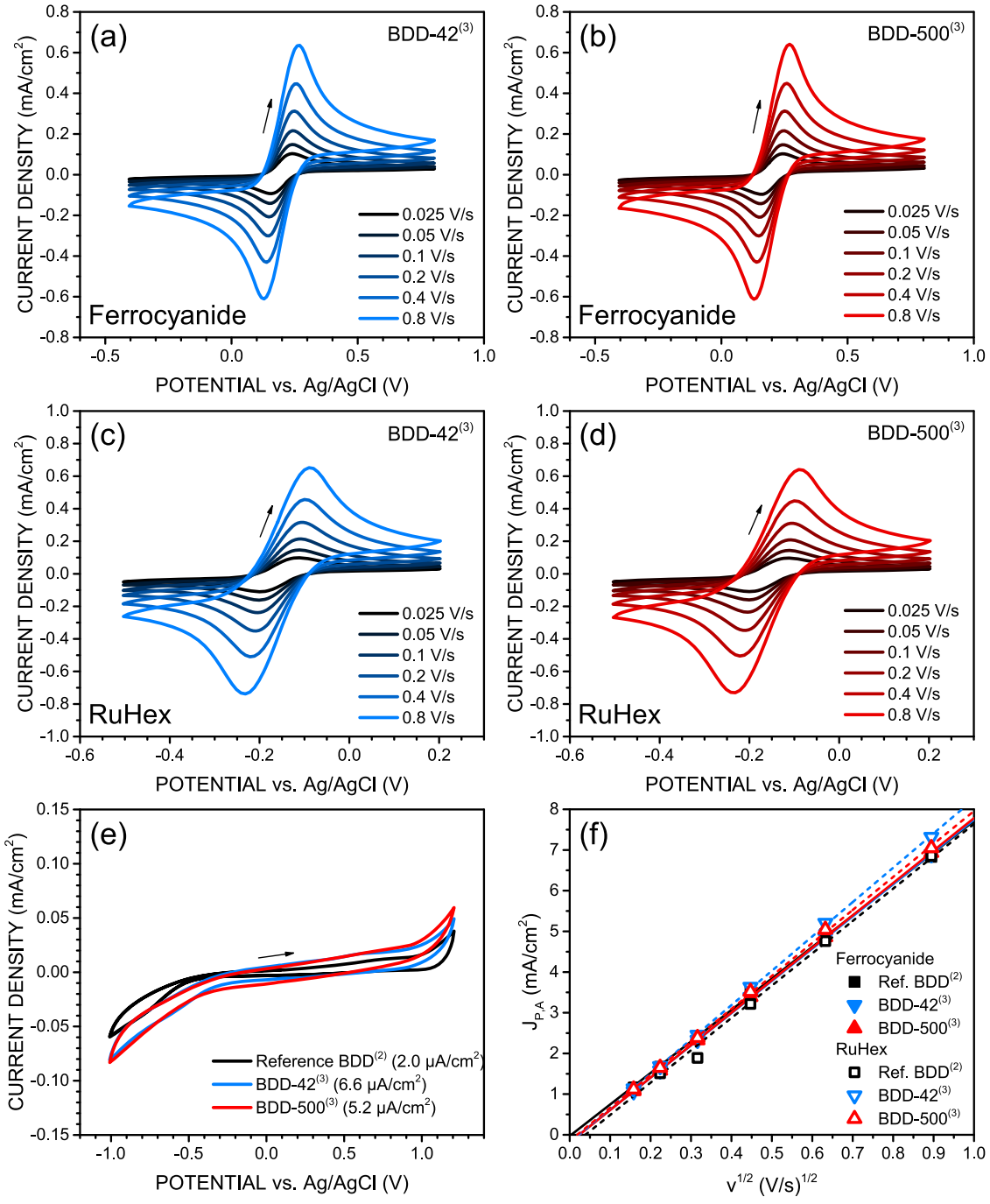


**Figure 8.** Effect of strong polarization in $HNO_3$ on the subsequent electrochemical behavior of the laser-textured samples. (a, b) Cyclic voltammograms in 0.1 M KCl aqueous solution containing 1 mM $Fe(CN)_6^{3-/4-}$ at different scan rates. (c, d) Cyclic voltammograms in 0.1 M KCl aqueous solution containing 1 mM $Ru(NH_3)_6^{3+/2+}$ at different scan rates. (e) Cyclic voltammograms in 0.1 M KCl aqueous solution without redox couple. Each curve corresponds to the 10th cycle. (f) Relationship between anodic peak current density and square root of the scan rate, for each sample, for both redox couples. The linearity was high in all cases, with all $r^2$ above 0.99.

500 (high accumulated fluence). In both cases, the nanostructured, rippled surfaces can be clearly distinguished from the underlying BDD. The depth of the laser-textured surface is roughly in the range of 100 nm, similar for both low and high accumulated fluences. Figure 10c,f shows the respective surfaces after strong polarization in nitric acid, revealing the diamond structure that was left underneath the laser-textured surface. Both the morphology and image contrast show that the ripples were completely removed, exposing a BDD surface covered by scars arising from laser ablation, which are more prominent for the high-fluence treatment. Figure 10g schematically summarizes those observations discussed above.

## 4. DISCUSSION

**4.1. Laser Texturing.** The results from SEM and Raman spectroscopy indicate that the laser-texturing procedure for heavily B-doped diamond led to the formation of somewhat irregular quasi-periodic structures consisting of predominantly $sp^2$ carbon material. This is significantly different from the black diamond films previously obtained by laser-texturing


DOI: 10.1021/acsami.8b15951
ACS Appl. Mater. Interfaces 2018, 10, 43236−43251

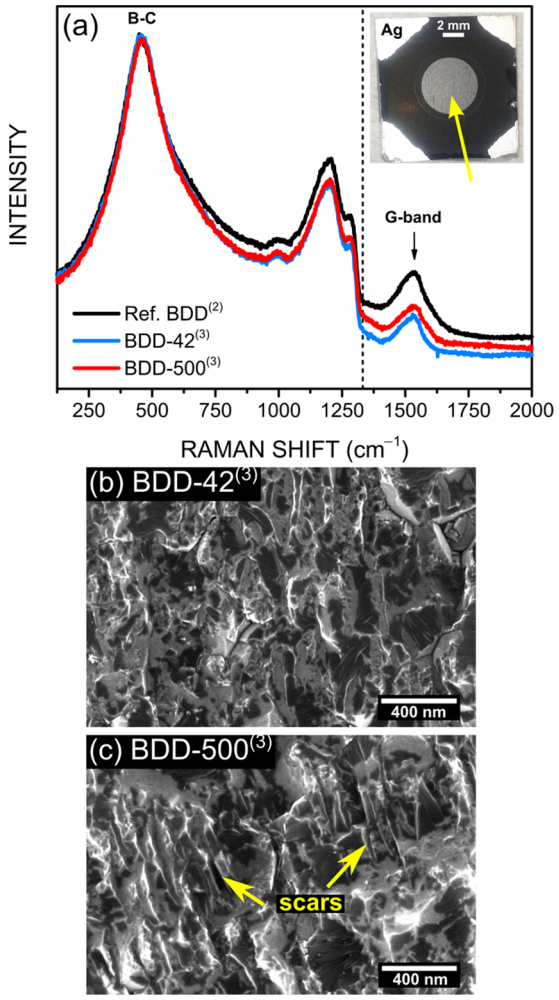


**Figure 9.** (a) Raman spectra of the laser-textured BDD samples after strong polarization in 0.1 M $HNO_3$. The spectrum of the acid-cleaned reference BDD was added for comparison. The dashed vertical line indicates the position of the (undoped) diamond one-phonon Raman line. The inset shows a photograph of the BDD-500 sample after the treatment, highlighting the physical change of the surface inside the active area (yellow arrow). (b, c) SEM images of (b) BDD-42 and (c) BDD-500 after polarization in $HNO_3$.

polished, optical-grade polycrystalline diamond,[27] where the ripple formation was achieved with far higher accumulated fluences (from 2.5 to 12.5 kJ/cm$^2$ versus 0.014 to 0.410 kJ/cm$^2$ in this work) and consisted of more regular structures without the presence of sp$^2$ carbon after acid cleaning. In the report from Granados et al.,[29] where polished BDD with lower doping level was used (~0.01 atom % compared to ~2.8 atom % in this work), the formation of ripples was achieved starting from laser accumulated fluences of ~2 kJ/cm$^2$, which is consistent with the observations on undoped diamond.[27,29] Our results thus indicate that heavily B-doped diamond undergoes a different mechanism of LIPSS formation than diamond with lower doping concentrations, likely due to a combination of optical and material properties: on the one hand, heavily boron-doped diamond is reported to show an unusually high extinction coefficient in the visible to near-infrared region,[51] causing the incident laser energy to be absorbed in a smaller volume of the BDD surface. The higher local energy density, further helped by BDD's lower thermal conductivity,[52] is thus sufficient to initiate graphitization of the diamond at lower laser fluences. On the other hand, heavily boron-doped diamond is also known to be a softer material. In a previous work,[53] we showed that both the hardness and elastic modulus of BDD films with 2.8 atom % [B/C] were roughly 2 times smaller than in the case of 0.6 atom %. The wear rate of BDD films was found to increase proportionally with the doping level, with the 2.8 atom % films wearing at least 3 times faster than the 0.6 atom % ones. Thus, we attribute the formation of the observed sp$^2$ carbon-rich ripples in the present work to the particular optical and material properties of heavily B-doped diamond films, which may translate into a lower ablation threshold for this material than for diamond of lower doping levels. In a recent work by Cadot et al.,[54] the ablation of BDD (with lower [B]) by a single nanosecond laser pulse (30 ns, 1064 nm wavelength) was studied theoretically and experimentally. They reported that BDD undergoes a thermally driven graphitization process, with the formation of a nanocrystalline graphite layer at low fluences (<30 J/cm$^2$), which transforms into an amorphous layer at higher fluences, due to melting. A higher degree of disorder of the graphitized layer was observed near the surface, which is coherent with our observations from Raman spectroscopy before and after acid cleaning (Figure 2). Overall, despite the laser ablation conditions in their work being significantly different from the present work, the results further support our observations that LIPSS on heavily boron-doped diamond induces a stronger graphitization of the surface.

The graphitic nature of the ripples was further confirmed by the effect of strong polarization in nitric acid. This process is known to induce the removal of active sp$^2$ carbon material from the electrode surface, presumably by oxidative dissolution or complete "burning" into $CO_2$, with the etch rate being proportional to the relative sp$^2$/sp$^3$ content exposed to the electrolyte.[49,55] The Raman and SEM results shown in Figures 9 and 10c,f, respectively, measured after polarization in nitric acid, clearly show the removal of the sp$^2$ carbon ripples, exposing features of a predominant diamond surface. The Raman spectra of both low- and high-fluence samples were identical to each other and nearly identical to the reference BDD, presenting the same features. The SEM images, however, still show an electronic contrast, which suggests the existence of leftovers from the sp$^2$ carbon layer that were not fully removed by the nitric acid procedure and which may be responsible for the improved electrochemical performance of the electrodes, as seen from the kinetic parameters measured in ferrocyanide (Table 2) and RuHex (Table 3). This is supported by the visible C=C (sp$^2$) shoulder in the XPS spectra of the laser-textured samples after polarization in $HNO_3$, shown in Figure 7.

**4.2. Electrochemical Performance.** Overall, the laser-texturing process with the formation of sp$^2$ carbon led to slightly slower electrode kinetics for ferrocyanide, for both low and high fluences, as can be seen in Table 2 and Figure S5 (i.e., lower peak currents in the voltammograms). That is somewhat surprising, given that the presence of sp$^2$ carbon is known to efficiently catalyze electron transfer on glassy carbon or highly oriented pyrolytic graphite (HOPG) electrodes.[56,57] Diamond electrodes with high-phase purity are not favorable for the redox reaction of ferrocyanide, as it exhibits inner-sphere electron transfer and relies on the presence of specific adsorbates, chemical sites, and surface termination[58−60] to catalyze electron transfer. Thus, we attribute the observed slower kinetics after laser texturing to two possible reasons: (1)


DOI: 10.1021/acsami.8b15951
ACS Appl. Mater. Interfaces 2018, 10, 43236−43251

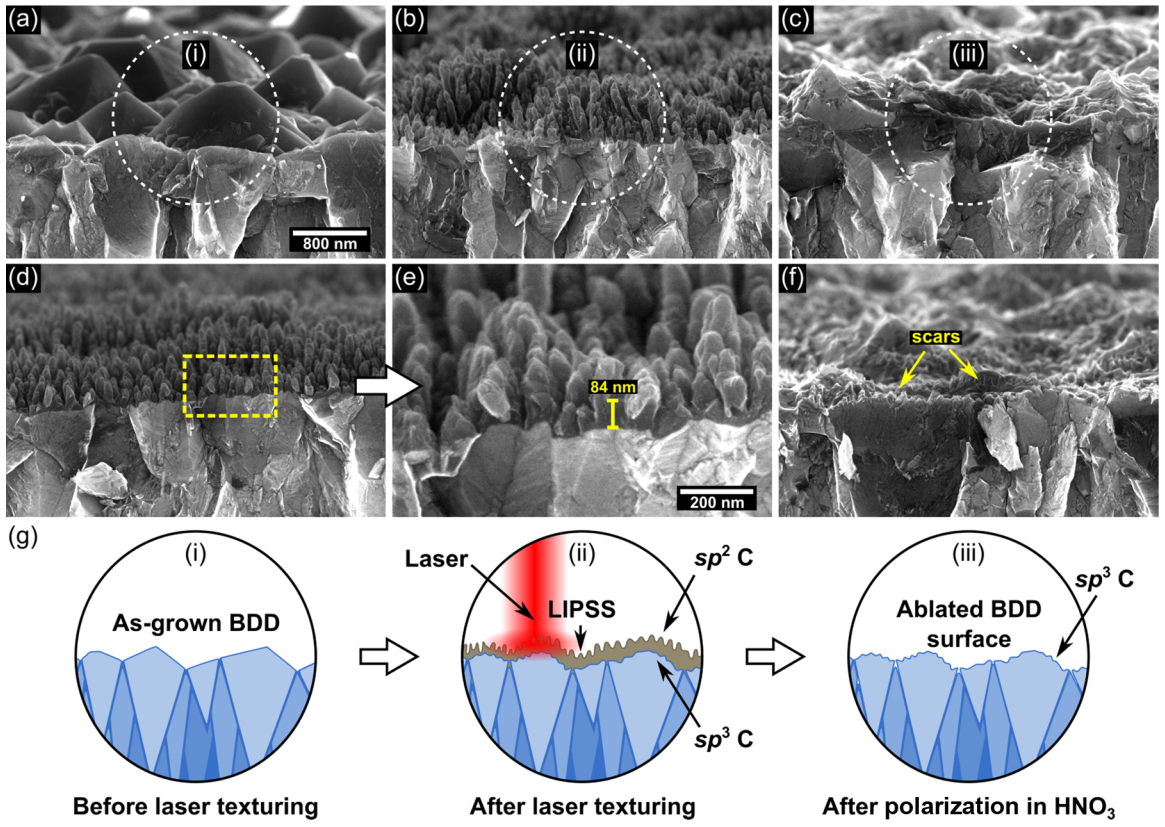


**Figure 10.** Cross-sectional SEM images of (a) reference BDD (i.e., before texturing), (b) BDD-42 (low accumulated fluence) sample after texturing and acid cleaning, (c) BDD-42 after strong polarization in 0.1 M $HNO_3$, (d) BDD-500 (high accumulated fluence) sample after texturing and acid cleaning, (e) higher magnification of (d), and (f) BDD-500 after strong polarization in 0.1 M $HNO_3$. The images were acquired with 10° tilt toward the surface. Images are at the same scale, except for (e). (g) Schematic description of (a), (b), and (c), respectively, in (i), (ii), and (iii).

the presence of debris partially obstructing the surface, on the one hand, and (2) the reconstruction of the surface into (likely amorphous) forms that are not electrochemically active, as the laser-texturing process was carried out in vacuum (i.e., no oxygen, no hydrogen). This hypothesis is supported by the fact that the electrochemical behavior of the laser-textured samples in RuHex was more similar to the behavior of the reference BDD, considering the overall picture from the CV and EIS data shown in Table 3 and Figure S6. As RuHex undergoes outer-sphere electron transfer on carbon electrodes and is mainly affected by surface conductivity,[58] the lack of chemically active sites did not hinder electron transfer. The electrode performance in RuHex thus indicates that the surface conductivity was not negatively affected by the laser-texturing process.

After acid cleaning, which is a strongly oxidative process, the electron-transfer kinetics in ferrocyanide improved for both laser-textured samples (see Table 2), likely due to the partial removal of amorphous carbon and to the activation of the surface with functional groups (e.g., hydroxyl, carboxyl) and aromatic compounds that were not present before, as indicated by XPS measurements (Figure 7). The most striking change, however, was the massive increase in background current of the BDD-500 (high-fluence sample), by more than 3-fold, whereas the background current of the low-fluence sample remained effectively unchanged (see Figure 4). As suggested by the Raman spectra and SEM images taken in this state (see Figure 2), we argue that both the improvement in kinetics for ferrocyanide and the increase in background current were caused by a combination of material removal and surface functionalization. The boiling concentrated $H_2SO_4$ and $HNO_3$ etched away weakly bound $sp^2$ carbon debris and likely also a certain fraction of the ripples themselves, contributing to an increase of the electroactive area, particularly of the high-fluence sample, while at the same time creating chemically active sites for the redox reaction of ferrocyanide. The effect of acid cleaning on the electrochemical behavior in RuHex, on the other hand, is less clear, likely due to the uncertainties discussed in Section 3.2.2. There, the cyclic voltammetry analysis suggests worse kinetics for BDD-500 and better for BDD-42, whereas the impedance analysis suggests improved kinetics for both, thus pointing to improved conductivity (see Table 3). However, the substantial increase in double-layer capacitance after acid cleaning was also evident in RuHex (see Figure 5).

The analysis of all laser-textured samples revealed a clear relationship between the full width at half-maximum of the D- and G-bands in the Raman spectra and the reversibility parameter, Λ, of the electrodes in ferrocyanide after acid cleaning, as shown in Figure S8 (Supporting Information). The lower the degree of disorder of the surface (i.e., from amorphous to graphitic), the higher the electrode kinetics, with BDD-42 and BDD-500 showing the best performances.

After polarization in $HNO_3$, both electrodes showed improved kinetics for ferrocyanide (even better than the reference BDD) and comparable kinetics to the reference BDD for RuHex. The effect can be explained as a consequence of excess amorphous carbon material formed by the laser ablation


DOI: 10.1021/acsami.8b15951
ACS Appl. Mater. Interfaces 2018, 10, 43236−43251

process being removed from the surface of the diamond. This amorphous material decreased electrode kinetics, as seen earlier for both laser-textured samples before and after acid cleaning. However, as indicated by the $sp^2$ shoulder on the XPS images in Figure 7, the electrodes after polarization in $HNO_3$ still contain a small percentage of nondiamond phase, which likely catalyzes the redox reaction of ferrocyanide. The increase in electrode kinetics suggests that controlled laser ablation of the BDD surface could be used as a strategy to enhance its sensitivity and tune its selectivity toward specific redox couples and thus enhance the performance of BDD applied as electrochemical (bio)sensor.

**4.3. Electrode Performance for Cell Stimulation and Energy Storage.** The most prominent effect of laser texturing on the BDD electrodes was the huge increase in capacitive charging, which is a very important electrode property for cell stimulation and recording[61,62] and for applications as supercapacitors.[12,13] Diamond has been of particular interest for such applications due to its biocompatibility and chemical inertness. However, its inherent low dielectric constant, which is an advantage for (bio)electrochemical sensing, is a disadvantage for cell stimulation and electrochemical supercapacitors. This has led to the investigation of different surface nanostructuring routes to increase the electroactive area and thus enhance charge-storage capacity (CSC), most of them consisting of coating carbon nanotube (CNT), polymeric or other scaffolds with diamond,[11,13,16] or producing nanowires.[12,15] These approaches have the disadvantages of being complex to fabricate and require the use of materials that are foreign to the diamond electrode, such as polypyrrole, which may suffer from issues with diamond seeding and growth (i.e., incomplete coating) and poor long-term stability. All of these issues can be avoided with laser texturing, as LIPSS can be performed locally at the desired electrode location, quickly and in one step, creating the required all-carbon nanostructures on the electrode surface without complexity. Indeed, the results in Figure 11 confirm that laser texturing can significantly enhance the CSC. The left axis displays the same voltammograms from Figure 3 as a function of time, whereas the right axis shows the total charge (sum of anodic and cathodic currents), $CSC_{tot} = CSC_a + CSC_c$, from the integrated voltammograms. Laser texturing at high accumulated fluence led to >6-fold increase of total CSC compared to the untreated reference sample, from 0.5 to 3.2 $mC/cm^2$. This is, to the best of our knowledge, the first report of CSC for laser-textured BDD and also the highest reported value for a modified BDD surface without the use of scaffolds (see Table 4). The laser-textured BDD also performed remarkably well compared to the highly surface-enhanced BDD foam/paper reported by Gao et al.[13] applied as supercapacitor: with a much lower electroactive area and single-step surface texturing, we obtained a comparable double-layer capacitance of roughly 0.7 $mF/cm^2$ at only 0.1 V/s (see Table 4).

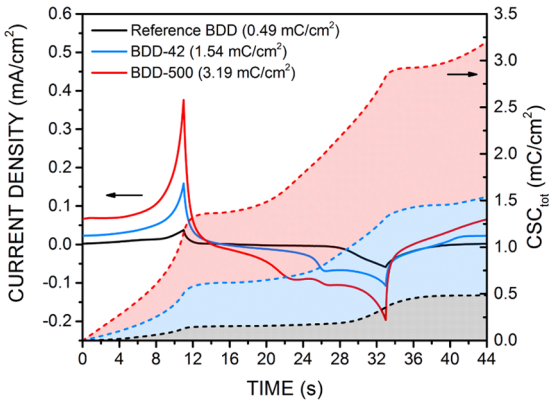


**Figure 11.** Time-dependent voltammograms (left axis) and total charge-storage capacity (right axis) of the laser-textured samples BDD-42 (low accumulated fluence), BDD-500 (high accumulated fluence), and reference BDD, all after acid cleaning, measured in 0.1 M KCl aqueous solution at 0.1 V/s scan rate. Each curve corresponds to the 10th cycle.

The second important electrode parameter is the impedance, which should be low to enable signal collection and recording,[63] as well as fast charging/discharging. The summary in Table 4 shows the normalized impedance (i.e., $|Z| \times A$), measured at 1 kHz, of a few reported microelectrodes. The values are typically in the order of a few Ω $cm^2$, while a state-of-the-art value of 0.16 Ω $cm^2$ for diamond[11] was achieved using CNT scaffold onto a $3.14 \times 10^{-6}$ $cm^2$ BDD microelectrode, thus leading to a much higher electroactive area. There, the bare BDD with the same geometric area led to an impedance value of 3.14 Ω $cm^2$, which is in the same range as for other nondiamond, high-surface-area polymer/CNT composite materials.[63] In the present work, the measured $|Z|$ at 1 kHz for the high-fluence laser-textured sample was 195 Ω, which corresponds to the total series resistance of the circuit, including the electrolyte resistance, as was systematically measured by EIS in ferrocyanide and RuHex (see Section 3.3). This is because we employed a relatively large-scale electrochemical setup, instead of a closely spaced cell or microelectrode configuration. As the impedance modulus curve was flat from $10^1$ to $10^5$ Hz (see Figure S9 in the Supporting Information), the real electrode impedance can be approximated to its bulk resistance of 12.5 Ω (i.e., 2.74 Ω $cm^2$). This competitive value, together with the high CSC, makes laser texturing a viable and attractive route for the low-cost fabrication of nanostructured diamond electrodes for cell stimulation/recording and energy storage.

## 5. CONCLUSIONS

In summary, we reported a comprehensive characterization of the electrochemical and morphological/structural properties of laser-induced periodic surface structures (LIPSS) formed on heavily boron-doped CVD diamond (BDD). We observed LIPSS formation on this material at much lower accumulated fluences than the 2 $kJ/cm^2$ typically used for diamond with lower doping levels. This was attributed to stronger laser energy absorption at the BDD surface, as well as to the lower hardness and elastic modulus of heavily B-doped diamond. The LIPSS process led to the formation of $sp^2$ carbon-rich surfaces, with a high accumulated fluence of 0.325 $kJ/cm^2$ leading to a more regular and periodic rippled morphology than the low accumulated fluence of 0.027 $kJ/cm^2$. Cyclic voltammetry and impedance spectroscopy measurements in ferrocyanide and RuHex enabled the quantification of electrode kinetics in several electrode states, i.e., (1) as-textured, (2) after acid cleaning, and (3) after removing the ripples with strong cycling in nitric acid. The laser-texturing process led to slower kinetics for ferrocyanide, relative to the untreated BDD, despite the increased $sp^2$ carbon content on the surface. The acid cleaning treatment improved the electrode performance through partial etching of $sp^2$ carbon,


DOI: 10.1021/acsami.8b15951
ACS Appl. Mater. Interfaces 2018, 10, 43236−43251

**Table 4. Comparison of Several Reported Electrode Properties**

| material | $C_{dl}$ (mF/cm$^2$) | $CSC_{a/c}$ (mC/cm$^2$) | scan rate (V/s) | potential window (V) | electrolyte | 1 kHz \|Z\| (Ω cm$^2$) |
|---|---|---|---|---|---|---|
| diamond | | | | | | |
| BDD[11] | 0.07 | 0.22 | 0.1 | 3.3 | $LiClO_4$ | 3.14 |
| CNT/BDD[11] | 3 | 10 | 0.1 | 3.3 | $LiClO_4$ | 0.16 |
| PPy/NCD[16] | 3 | 53 | 0.1 | 2.8 | $LiClO_4$ | |
| N-UNCD[62] | | 0.3 | | 2.9 | PBS | |
| BDD paper[13] | 0.69 | | 1 | 2.5 | $NaClO_4$ | 1.95[c] |
| **this work**[a] | 0.66 | 1.6 ± 0.1 | 0.1 | 2.1 | KCl | 2.74 |
| others | | | | | | |
| PEDOT[64] | | 75 | 0.05 | 1.3 | PBS | 0.095 |
| $IrO_x$[64] | | 28 | 0.05 | 1.4 | PBS | 0.47 |
| PPy/CNT[63] | | 67.7[b] | 0.1 | 1.6 | NaCl | 3.88 |
| PEDOT/CNT[63] | | 92.3[b] | 0.1 | 1.6 | NaCl | 4.25 |

[a]Parameters from the high-fluence sample BDD-500. [b]Total charge-storage capacity, which is roughly twice the anodic/cathodic charge-storage capacity, $CSC_{a/c}$. [c]Roughly estimated.

by exposing graphitic material with higher crystallinity and by activating the surface with chemically active sites. The best electrode performance was achieved after step (3), by exposing the ablated diamond surface directly to the solution, which suggests that the controlled laser ablation of the BDD surface can be used to enhance its sensitivity and selectivity toward specific analytes for electrochemical (bio)sensing. Overall, the LIPSS process had a significant impact on the double-layer capacitance, $C_{dl}$: the formation of ripples with a high laser accumulated fluence of 0.325 kJ/cm$^2$ led to an increase in $C_{dl}$ from 20 μF/cm$^2$ for the untreated BDD up to 660 μF/cm$^2$ for the laser-textured BDD. As a consequence, the anodic/cathodic charge-storage capacity increased from 0.5 to 1.6 mC/cm$^2$ after laser texturing. A general trend of increasing capacitance for increasing laser fluence was observed, with the highest fluence of 0.410 kJ/cm$^2$ leading to 1080 μF/cm$^2$. Impedance spectroscopy measurements in RuHex showed an increase in capacitance of the high-fluence electrode up to a factor of ∼3, while measurements in ferrocyanide yielded a factor of up to ∼40. Together with a low impedance of 2.74 Ω cm$^2$, the high-fluence laser-textured BDD with its enhanced capacitive charging showed great potential as electrode for cell stimulation and energy storage as supercapacitors.

Overall, we demonstrated that LIPSS is a promising, scalable, cleanroom-free, and versatile method for the modification of the electrochemical properties of boron-doped diamond. This technique allows the simultaneous manipulation of the electroactive area, as well as the chemical nature of the diamond surface by introducing sp$^2$ carbon phases. If performed in controlled atmosphere (i.e., containing $O_2$, $H_2$, or other gases), LIPSS process on BDD has the potential to promote in situ surface functionalization with a wider range of functional groups. Combining that with further optimization of laser-texturing conditions (e.g., laser wavelength, pulse energy, etc.), as well as double texturing by scanning the laser beam in orthogonal directions,[26] LIPSS is expected to enable an even greater degree of control over the electrochemical properties of carbon electrodes in general and lead to future BDD electrodes with higher charge-storage/injection figures and enhanced sensing performance for specific target molecules, such as dopamine, paracetamol, glucose, and others.

## ■ ASSOCIATED CONTENT

### Supporting Information

The Supporting Information is available free of charge on the ACS Publications website at DOI: 10.1021/acsami.8b15951.

Additional experimental details pertaining to the LIPSS process, electrochemical setup, and XPS analysis; description of the laser-texturing parameters for all samples; additional SEM and Raman spectroscopy data from all of the laser-textured samples; contact angle measurement; cyclic voltammograms for the as-textured samples (before acid cleaning); and additional XPS and EIS data (PDF)

## ■ AUTHOR INFORMATION


### Corresponding Authors

*E-mail: A.FrotaSartori@tudelft.nl. Tel.: +31 (0)15 27 86089 (A.F.S.).

*E-mail: J.G.Buijnsters@tudelft.nl. Tel.: +31 (0)15 27 85396 (J.G.B).

### ORCID

André F. Sartori: 0000-0002-6789-5342


### Notes

The authors declare no competing financial interest.

## ■ ACKNOWLEDGMENTS

The authors acknowledge Agnieszka Kooijman for her kind assistance with contact angle measurements.

## ■ SYMBOLS

Symbol, unit, Description

α, 0−1, transfer coefficient from Butler−Volmer theory of charge transfer in an electrochemical cell

$A$, cm$^2$, geometric area of the electrodes

$C_{dl}$, μF/cm$^2$, double-layer capacitance

$C_{dl\ eq.}$, μF/cm$^2$, equivalent double-layer capacitance estimated from the constant-phase element

$CSC_{a/c}$, mC/cm$^2$, anodic/cathodic charge-storage capacity

$CSC_{tot}$, mC/cm$^2$, total charge-storage capacity

$D$, cm$^2$/s, diffusion coefficient of species near the electrode surface

$F$, C/mol, Faraday constant

Λ, figure of merit for the reversibility of electrode kinetics

$i$, mA, current



DOI: 10.1021/acsami.8b15951
ACS Appl. Mater. Interfaces 2018, 10, 43236−43251

$j$, mA/cm$^2$, current density
$J_{P,A}$, mA/cm$^2$, anodic peak current density
$k_0$, $\mu$m/s, electron-transfer rate
$\lambda$, nm, wavelength of the laser incident on the sample
$n$, index of refraction of diamond
$n_Q$, (0−1), ideality factor of the constant-phase impedance element
$n_W$, (0−1), phase of the Warburg element (≈0.5 for 45° phase)
$Q_0$, s$^n$/Ω, coefficient of the constant-phase element (pseudocapacitance), with units in seconds to the $n_W$th power per Ohm
$r^2$, (0−1), adjusted coefficient of determination
$R$, J/(mol K), ideal gas constant
$R_{CT}$, Ω, charge-transfer resistance
$R_S$, Ω, bulk series resistance
$T$, K, absolute temperature
$V_0$, mV, formal potential
$\Delta V_P$, mV, peak−peak separation, i.e., $V_{P,A}-V_{P,C}$
$V_{P,A}$, mV, anodic peak potential
$V_{P,C}$, mV, cathodic peak potential
$v$, V/s, potential scan rate applied in cyclic voltammetry measurements
$v_r$, mm/s, raster speed of the laser spot across the sample surface
$W_0$, s$^{1/2}$/Ω, Warburg coefficient of the Warburg impedance element
$\chi^2$, sum of weighted squares of residuals from the impedance fitting
$|Z|$, Ω cm$^2$, normalized impedance modulus
$\omega_{max}$, rad, frequency at which the Im($Z$) is at its maximum

## REFERENCES


(1) Gicquel, A.; Hassouni, K.; Silva, F.; Achard, J. CVD Diamond Films: From Growth to Applications. *Curr. Appl. Phys.* **2001**, *1*, 479−496.
(2) Nebel, C. E. Electronic Properties of CVD Diamond. *Semicond. Sci. Technol.* **2003**, *18*, S1−S11.
(3) Szunerits, S.; Nebel, C. E.; Hamers, R. J. Surface Functionalization and Biological Applications of CVD Diamond. *MRS Bull.* **2014**, *39*, 517−524.
(4) Childress, L.; Hanson, R. Diamond NV Centers for Quantum Computing and Quantum Networks. *MRS Bull.* **2013**, *38*, 134−138.
(5) Riedrich-Möller, J.; Kipfstuhl, L.; Hepp, C.; Neu, E.; Pauly, C.; Mucklich, F.; Baur, A.; Wandt, M.; Wolff, S.; Fischer, M.; Gsell, S.; Schreck, M.; Becher, C. One- and Two-Dimensional Photonic Crystal Microcavities in Single Crystal Diamond. *Nat. Nanotechnol.* **2012**, *7*, 69−74.
(6) Wort, C. J. H.; Balmer, R. S. Diamond as an Electronic Material. *Mater. Today* **2008**, *11*, 22−28.
(7) Buja, F.; Kokorian, J.; Sumant, A. V.; van Spengen, W. M. Studies on Measuring Surface Adhesion between Sidewalls in Boron Doped Ultrananocrystalline Diamond Based Microelectromechanical Devices. *Diamond Relat. Mater.* **2015**, *55*, 22−31.
(8) Sumant, A. V.; Auciello, O.; Liao, M.; Williams, O. A. MEMS/NEMS Based on Mono-, Nano-, and Ultrananocrystalline Diamond Films. *MRS Bull.* **2014**, *39*, 511−516.
(9) Taylor, A. C.; Vagaska, B.; Edgington, R.; Hébert, C.; Ferretti, P.; Bergonzo, P.; Jackman, R. B. Biocompatibility of Nanostructured Boron Doped Diamond for the Attachment and Proliferation of Human Neural Stem Cells. *J. Neural Eng.* **2015**, *12*, No. 066016.
(10) Nebel, C. E.; Shin, D.; Rezek, B.; Tokuda, N.; Uetsuka, H.; Watanabe, H. Diamond and Biology. *J. R. Soc. Interface* **2007**, *4*, 439−461.
(11) Piret, G.; Hébert, C.; Mazellier, J.-P.; Rousseau, L.; Scorsone, E.; Cottance, M.; Lissorgues, G.; Heuschkel, M. O.; Picaud, S.; Bergonzo, P.; Yvert, B. 3D-Nanostructured Boron-Doped Diamond for Microelectrode Array Neural Interfacing. *Biomaterials* **2015**, *53*, 173−183.
(12) Aradilla, D.; Gao, F.; Lewes-Malandrakis, G.; Müller-Sebert, W.; Gentile, P.; Boniface, M.; Aldakov, D.; Iliev, B.; Schubert, T. J. S.; Nebel, C. E.; Bidan, G. Designing 3D Multihierarchical Heteronanostructures for High-Performance On-Chip Hybrid Supercapacitors: Poly(3,4-(Ethylenedioxy)Thiophene)-Coated Diamond/Silicon Nanowire Electrodes in an Aprotic Ionic Liquid. *ACS Appl. Mater. Interfaces* **2016**, *8*, 18069−18077.
(13) Gao, F.; Nebel, C. E. Diamond-Based Supercapacitors: Realization and Properties. *ACS Appl. Mater. Interfaces* **2016**, *8*, 28244−28254.
(14) Hébert, C.; Scorsone, E.; Bendali, A.; Kiran, R.; Cottance, M.; Girard, H. A.; Degardin, J.; Dubus, E.; Lissorgues, G.; Rousseau, L.; Mailley, P.; Picaud, S.; Bergonzo, P. Boron Doped Diamond Biotechnology: From Sensors to Neurointerfaces. *Faraday Discuss.* **2014**, *172*, 47−59.
(15) Yang, N.; Foord, J. S.; Jiang, X. Diamond Electrochemistry at the Nanoscale: A Review. *Carbon* **2016**, *99*, 90−110.
(16) Hébert, C.; Scorsone, E.; Mermoux, M.; Bergonzo, P. Porous Diamond with High Electrochemical Performance. *Carbon* **2015**, *90*, 102−109.
(17) Aramesh, M.; Fox, K.; Lau, D. W. M.; Fang, J.; Ostrikov, K.; Prawer, S.; Cervenka, J. Multifunctional Three-Dimensional Nanodiamond-Nanoporous Alumina Nanoarchitectures. *Carbon* **2014**, *75*, 452−464.
(18) Nemanich, R. J.; Carlisle, J. A.; Hirata, A.; Haenen, K. CVD Diamond - Research, Applications, and Challenges. *MRS Bull.* **2014**, *39*, 490−494.
(19) Bonse, J.; Höhm, S.; Kirner, S. V.; Rosenfeld, A.; Krüger, J. Laser-Induced Periodic Surface Structures - A Scientific Evergreen. *IEEE J. Sel. Top. Quantum Electron.* **2017**, *23*, 109−123.
(20) Trucchi, D.; Bellucci, A.; Girolami, M.; Mastellone, M.; Orlando, S. Surface Texturing of CVD Diamond Assisted by Ultrashort Laser Pulses. *Coatings* **2017**, *7*, 185.
(21) Parmar, V.; Shin, Y. C. Wideband Anti-Reflective Silicon Surface Structures Fabricated by Femtosecond Laser Texturing. *Appl. Surf. Sci.* **2018**, *459*, 86−91.
(22) Ta, V. D.; Dunn, A.; Wasley, T. J.; Li, J.; Kay, R. W.; Stringer, J.; Smith, P. J.; Esenturk, E.; Connaughton, C.; Shephard, J. D. Laser Textured Superhydrophobic Surfaces and Their Applications for Homogeneous Spot Deposition. *Appl. Surf. Sci.* **2016**, *365*, 153−159.
(23) Müller, F.; Kunz, C.; Gräf, S. Bio-Inspired Functional Surfaces Based on Laser-Induced Periodic Surface Structures. *Materials* **2016**, *9*, 476.
(24) Ozkan, A. M.; Malshe, A. P.; Railkar, T. A.; Brown, W. D.; Shirk, M. D.; Molian, P. A. Femtosecond Laser-Induced Periodic Structure Writing on Diamond Crystals and Microclusters. *Appl. Phys. Lett.* **1999**, *75*, 3716−3718.
(25) Calvani, P.; Bellucci, A.; Girolami, M.; Orlando, S.; Valentini, V.; Lettino, A.; Trucchi, D. M. Optical Properties of Femtosecond Laser-Treated Diamond. *Appl. Phys. A* **2014**, *117*, 25−29.
(26) Bellucci, A.; Calvani, P.; Girolami, M.; Orlando, S.; Polini, R.; Trucchi, D. M. Optimization of Black Diamond Films for Solar Energy Conversion. *Appl. Surf. Sci.* **2016**, *380*, 8−11.
(27) Calvani, P.; Bellucci, A.; Girolami, M.; Orlando, S.; Valentini, V.; Polini, R.; Trucchi, D. M. Black Diamond for Solar Energy Conversion. *Carbon* **2016**, *105*, 401−407.
(28) Rehman, Z. U.; Janulewicz, K. A. Structural Transformation of Monocrystalline Diamond Driven by Ultrashort Laser Pulses. *Diamond Relat. Mater.* **2016**, *70*, 194−200.
(29) Granados, E.; Calderon, M. M.; Krzywinski, J.; Wörner, E.; Rodriguez, A.; Aranzadi, M. G.; Olaizola, S. M. Enhancement of Surface Area and Wettability Properties of Boron Doped Diamond by Femtosecond Laser-Induced Periodic Surface Structuring. *Opt. Mater. Express* **2017**, *7*, 3389−3396.
(30) Komlenok, M. S.; Dezhkina, M. A.; Kononenko, V. V.; Khomich, A. A.; Popovich, A. F.; Konov, V. I. Effect of Laser



DOI: 10.1021/acsami.8b15951
*ACS Appl. Mater. Interfaces* 2018, 10, 43236−43251

Radiation Parameters on the Conductivity of Structures Produced on the Polycrystalline Diamond Surface. *Bull. Lebedev Phys. Inst.* **2017**, *44*, 246−248.
(31) Granados, E.; Martinez-Calderon, M.; Gomez, M.; Rodriguez, A.; Olaizola, S. M. Photonic Structures in Diamond Based on Femtosecond UV Laser Induced Periodic Surface Structuring (LIPSS). *Opt. Express* **2017**, *25*, 15330−15335.
(32) Tsigkourakos, M.; Hantschel, T.; Janssens, S. D.; Haenen, K.; Vandervorst, W. Spin-Seeding Approach for Diamond Growth on Large Area Silicon-Wafer Substrates. *Phys. Status Solidi A* **2012**, *209*, 1659−1663.
(33) Zimmer, J.; Hantschel, T.; Chandler, G.; Vandervorst, W.; Peralta, M. Boron Doping in Hot Filament MCD and NCD Diamond Films. *MRS Proc.* **2011**, No. 1203.
(34) Kononenko, T. V.; Meier, M.; Komlenok, M. S.; Pimenov, S. M.; Romano, V.; Pashinin, V. P.; Konov, V. I. Microstructuring of Diamond Bulk by IR Femtosecond Laser Pulses. *Appl. Phys. A* **2008**, *90*, 645−651.
(35) Ushizawa, K.; Watanabe, K.; Ando, T.; Sakaguchi, I.; Nishitani-Gamo, M.; Sato, Y.; Kanda, H. Boron Concentration Dependence of Raman Spectra on {100} and {111} Facets of B-Doped CVD Diamond. *Diamond Relat. Mater.* **1998**, *7*, 1719−1722.
(36) Popova, D. M.; Mavrin, B. N.; Denisov, V. N.; Skryleva, E. A. Spectroscopic and First-Principles Studies of Boron-Doped Diamond: Raman Polarizability and Local Vibrational Bands. *Diamond Relat. Mater.* **2009**, *18*, 850−853.
(37) Ferrari, A. C.; Robertson, J. Interpretation of Raman Spectra of Disordered and Amorphous Carbon. *Phys. Rev. B* **2000**, *61*, 14095−14107.
(38) Merlen, A.; Buijnsters, J. G.; Pardanaud, C. A Guide to and Review of the Use of Multiwavelength Raman Spectroscopy for Characterizing Defective Aromatic Carbon Solids: From Graphene to Amorphous Carbons. *Coatings* **2017**, *7*, 153.
(39) Živcová, Z. V.; Frank, O.; Petrák, V.; Tarábková, H.; Vacík, J.; Nesládek, M.; Kavan, L. Electrochemistry and in Situ Raman Spectroelectrochemistry of Low and High Quality Boron Doped Diamond Layers in Aqueous Electrolyte Solution. *Electrochim. Acta* **2013**, *87*, 518−525.
(40) Trouillon, R.; O'Hare, D. Comparison of Glassy Carbon and Boron Doped Diamond Electrodes: Resistance to Biofouling. *Electrochim. Acta* **2010**, *55*, 6586−6595.
(41) Zoski, C. G. *Handbook of Electrochemistry*, 1st ed.; Elsevier, 2007.
(42) Nicholson, R. S. Theory and Application of Cyclic Voltammetry for Measurement of Electrode Reaction Kinetics. *Anal. Chem.* **1965**, *37*, 1351−1355.
(43) Cinková, K.; Batchelor-McAuley, C.; Marton, M.; Vojs, M.; Švorc, Ľ.; Compton, R. G. The Activity of Non-Metallic Boron-Doped Diamond Electrodes with Sub-Micron Scale Heterogeneity and the Role of the Morphology of Sp2 Impurities. *Carbon* **2016**, *110*, 148−154.
(44) Orazem, M. E.; Tribollet, B. The Electrochemical Society Series. In *Electrochemical Impedance Spectroscopy*; John Wiley & Sons, Inc., 2008.
(45) Lvovich, V. F. Impedance Representation of Bulk-Material and Electrode Processes. In *Impedance Spectroscopy*; John Wiley & Sons, Inc., 2012; pp 59−96.
(46) Hsu, C. H.; Mansfeld, F. Technical Note: Concerning the Conversion of the Constant Phase Element Parameter Y0 into a Capacitance. *Corrosion* **2001**, *57*, 747−748.
(47) Leiro, J. A.; Heinonen, M. H.; Laiho, T.; Batirev, I. G. Core-Level XPS Spectra of Fullerene, Highly Oriented Pyrolitic Graphite, and Glassy Carbon. *J. Electron Spectros. Relat. Phenomena* **2003**, *128*, 205−213.
(48) Liu, X.; Klauser, F.; Memmel, N.; Bertel, E.; Pichler, T.; Knupfer, M.; Kromka, A.; Steinmüller-Nethl, D. Spectroscopic Studies of Nanocrystalline Diamond Materials. *Diamond Relat. Mater.* **2007**, *16*, 1463−1470.
(49) Foord, J.; Hu, J. P. Electrochemical Oxidation and Reduction Processes at Diamond Electrodes of Varying Phase Purity. *Phys. Status Solidi A* **2006**, *203*, 3121−3127.
(50) Ryl, J.; Burczyk, L.; Bogdanowicz, R.; Sobaszek, M.; Darowicki, K. Study on Surface Termination of Boron-Doped Diamond Electrodes under Anodic Polarization in H2SO4 by Means of Dynamic Impedance Technique. *Carbon* **2016**, *96*, 1093−1105.
(51) Zimmer, A.; Williams, O. A.; Haenen, K.; Terryn, H. Optical Properties of Heavily Boron-Doped Nanocrystalline Diamond Films Studied by Spectroscopic Ellipsometry. *Appl. Phys. Lett.* **2008**, *93*, No. 131910.
(52) Prikhodko, D.; Tarelkin, S.; Bormashov, V.; Golovanov, A.; Kuznetsov, M.; Teteruk, D.; Volkov, A.; Buga, S. Thermal Conductivity of Synthetic Boron-Doped Single-Crystal HPHT Diamond from 20 to 400 K. *MRS Commun.* **2016**, *6*, 71−76.
(53) Buijnsters, J. G.; Tsigkourakos, M.; Hantschel, T.; Gomes, F. O. V.; Nuytten, T.; Favia, P.; Bender, H.; Arstila, K.; Celis, J.-P.; Vandervorst, W. Effect of Boron Doping on the Wear Behavior of the Growth and Nucleation Surfaces of Micro- and Nanocrystalline Diamond Films. *ACS Appl. Mater. Interfaces* **2016**, *8*, 26381−26391.
(54) Cadot, G. B. J.; Thomas, K.; Best, J. P.; Taylor, A. A.; Michler, J.; Axinte, D. A.; Billingham, J. Investigation of the Microstructure Change Due to Phase Transition in Nanosecond Pulsed Laser Processing of Diamond. *Carbon* **2018**, *127*, 349−365.
(55) Takarada, A.; Suzuki, T.; Kanda, K.; Niibe, M.; Nakano, M.; Ohtake, N.; Akasaka, H. Structural Dependence of Corrosion Resistance of Amorphous Carbon Films against Nitric Acid. *Diamond Relat. Mater.* **2015**, *51*, 49−54.
(56) McCreery, R. L.; Cline, K. K.; McDermott, C. A.; McDermott, M. T. Control of Reactivity at Carbon Electrode Surfaces. *Colloids Surf., A* **1994**, *93*, 211−219.
(57) Cline, K. K.; McDermott, M. T.; McCreery, R. L. Anomalously Slow Electron Transfer at Ordered Graphite Electrodes: Influence of Electronic Factors and Reactive Sites. *J. Phys. Chem.* **1994**, *98*, 5314−5319.
(58) Szunerits, S.; Boukherroub, R. Different Strategies for Functionalization of Diamond Surfaces. *J. Solid State Electrochem.* **2008**, *12*, 1205−1218.
(59) Duo, I.; Levy-Clement, C.; Fujishima, A.; Comninellis, C. Electron Transfer Kinetics on Boron-Doped Diamond Part I: Influence of Anodic Treatment. *J. Appl. Electrochem.* **2004**, *34*, 935−943.
(60) Ramesham, R. Cyclic Voltammetric Response of Boron-Doped Homoepitaxially Grown Single Crystal and Polycrystalline CVD Diamond. *Sens. Actuators, B* **1998**, *50*, 131−139.
(61) Cogan, S. F. Neural Stimulation and Recording Electrodes. *Annu. Rev. Biomed. Eng.* **2008**, *10*, 275−309.
(62) Hadjinicolaou, A. E.; Leung, R. T.; Garrett, D. J.; Ganesan, K.; Fox, K.; Nayagam, D. A. X.; Shivdasani, M. N.; Meffin, H.; Ibbotson, M. R.; Prawer, S.; O'Brien, B. J. Electrical Stimulation of Retinal Ganglion Cells with Diamond and the Development of an All Diamond Retinal Prosthesis. *Biomaterials* **2012**, *33*, 5812−5820.
(63) Castagnola, E.; Ansaldo, A.; Maggiolini, E.; Ius, T.; Skrap, M.; Ricci, D.; Fadiga, L. Smaller, Softer, Lower-Impedance Electrodes for Human Neuroprosthesis: A Pragmatic Approach. *Front. Neuroeng.* **2014**, *7*, No. 8.
(64) Wilks, S. J.; Richardson-Burn, S.; Hendricks, J.; Martin, D.; Otto, K. Poly(3,4-Ethylene Dioxythiophene) (PEDOT) as a Micro-Neural Interface Material for Electrostimulation. *Front. Neuroeng.* **2009**, *2*, No. 7.


DOI: 10.1021/acsami.8b15951
*ACS Appl. Mater. Interfaces* 2018, 10, 43236−43251